

AD-A096 550

DAVID W TAYLOR NAVAL SHIP RESEARCH AND DEVELOPMENT CE--ETC F/G 20/4
THE INFLUENCE OF HYDROFOIL OSCILLATION ON BOUNDARY LAYER TRANSI--ETC(U)
APR 81 Y T SHEN, F B PETERSON

UNCLASSIFIED

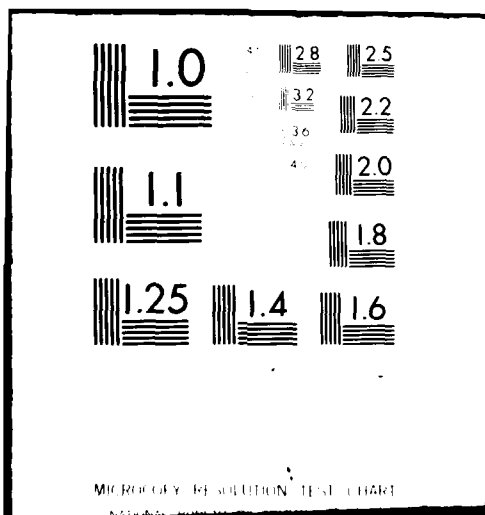
DTNSRDC-81/035

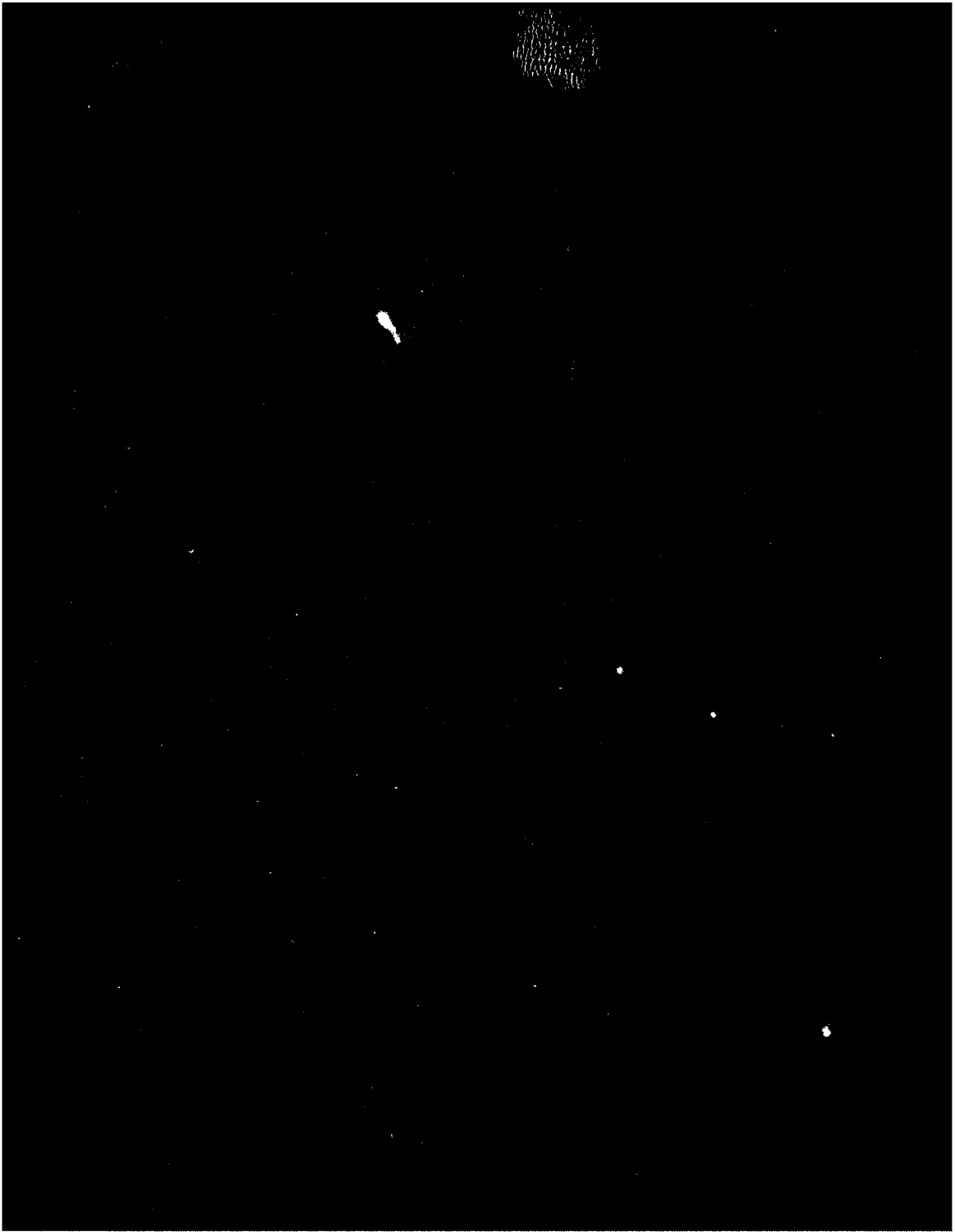
NL

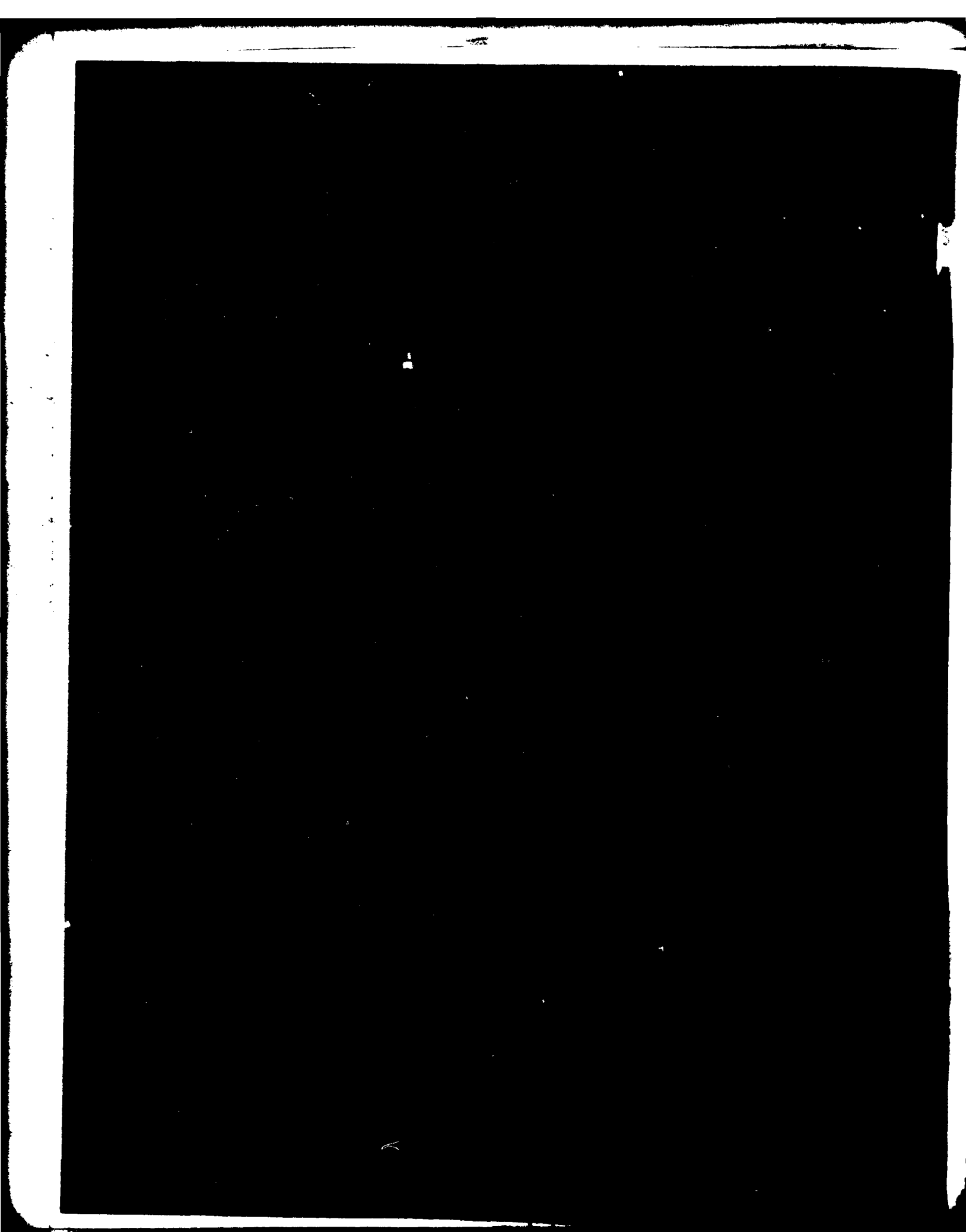
for
AD
201-453-500



END
DATE
FILMED
6-81
DTIC







UNCLASSIFIED

SECURITY CLASSIFICATION OF THIS PAGE (When Data Entered)

(Block 20 continued)

transducers were installed on the foil surface to measure pressure fluctuations and a hydrophone was used to measure the radiated cavitation noise. Two subjects are discussed in this paper: 1) relationship of boundary layer transition and pressure fluctuations with the hydrofoil in oscillation, and 2) noise generated by unsteady cavitation.

The magnitudes of pressure fluctuations in transition and turbulent regions are found to be independent of oscillation amplitude and frequency. However, the development of boundary layer and occurrence of transition are delayed with an increase in oscillation frequency. The influence of hydrofoil oscillation on cavitation inception is also discussed. With the occurrence of leading edge sheet cavitation, a significant effect of foil oscillation on cavitation noise is measured. At high reduced frequencies, extensive cloud cavitation is formed during the final phase of sheet cavity collapse and the noise level is significantly increased.

Accession For	
NTIS GRA&I	<input checked="" type="checkbox"/>
DTIC TAB	<input type="checkbox"/>
Unannounced	<input type="checkbox"/>
Justification for MP Conflict State on 7/1/71	
By _____	
Distribution/	
Availability Codes	
Dist Special	
A	

UNCLASSIFIED

SECURITY CLASSIFICATION OF THIS PAGE (When Data Entered)

TABLE OF CONTENTS

	Page
LIST OF FIGURES	iii
LIST OF TABLES.	vi
ABSTRACT.	1
PREFACE	1
INTRODUCTION.	1
EXPERIMENTAL APPARATUS AND TEST PROCEDURE	2
BOUNDARY LAYER PRESSURE FLUCTUATIONS ON A STATIONARY FOIL	3
BOUNDARY LAYER PRESSURE FLUCTUATIONS WITH FOIL IN OSCILLATION	7
INFLUENCE OF HYDROFOIL OSCILLATION ON CAVITATION INCEPTION.	13
CAVITATION INSTABILITY AND NOISE.	14
CONCLUDING REMARKS.	20
ACKNOWLEDGMENTS	20
REFERENCES.	21

LIST OF FIGURES

1 - Conceptual Design of Foil Oscillation Mechanism.	2
2 - Sequence of Ensemble Averaging	3
3 - Measured and Predicted Pressure Distributions.	4
4a - Computed Amplification Ratios at Foil Angle $\alpha = 3.25$ deg and $R_{nc} = 1.6 \times 10^6$	4
4b - Effect of Reynolds Numbers on Amplification Ratios at $\alpha = 3.25$ deg	4
5a - Measured Pressure Fluctuations at $R_{nc} = 1.2 \times 10^6$ in a Steady Flow at $\alpha = 3.25$	5
5b - Measured Pressure Fluctuations at $R_{nc} = 1.6 \times 10^6$ in a Steady Flow at $\alpha = 3.25$	5

	Page
5c - Measured Pressure Fluctuations at $R_{nc} = 2.4 \times 10^6$ in a Steady Flow at $\alpha = 3.25$	5
5d - Measured Pressure Fluctuations at $R_{nc} = 3.2 \times 10^6$ in a Steady Flow at $\alpha = 3.25$	5
5e - Measured Pressure Fluctuations at $R_{nc} = 3.6 \times 10^6$ in a Steady Flow at $\alpha = 3.25$	5
6 - Energy Spectrum of Run 8028 at $R_{nc} = 1.6 \times 10^6$	6
7 - Sample Oscillograph Record at $R_{nc} = 2.4 \times 10^6$, $f = 4$ Hz and $\alpha = 3.25 + 2.1 \sin \omega t$	7
8 - Measured RMS Pressure Fluctuations on Run 8043 at $R_{nc} = 2.4 \times 10^6$ and $\alpha = 3.25 + 2.1 \sin \omega t$	8
9 - Measured RMS Pressure Fluctuations at P_{10} with Oscillating Amplitude of 0.5 Degrees and $R_{nc} = 2.4 \times 10^6$	8
10 - Measured RMS Pressure Fluctuations at P_{10} with Oscillating Amplitude of 0.97 Degrees and $R_{nc} = 2.4 \times 10^6$	9
11 - Measured RMS Pressure Fluctuations at P_{10} with Oscillating Amplitude of 1.57 Degrees and $R_{nc} = 2.4 \times 10^6$	9
12 - Measured RMS Pressure Fluctuations at P_{10} with Oscillating Amplitude of 2.1 Degrees and $R_{nc} = 2.4 \times 10^6$	9
13 - Measured RMS Pressure Fluctuations at P_{25} with Oscillating Amplitude of 0.97 Degrees and $R_{nc} = 2.4 \times 10^6$	10
14 - Measured RMS Pressure Fluctuations at P_{25} with Oscillating Amplitude of 1.57 Degrees and $R_{nc} = 2.4 \times 10^6$	10
15 - Measured RMS Pressure Fluctuations at P_{25} with Oscillating Amplitude of 2.1 Degrees and $R_{nc} = 2.4 \times 10^6$	10
16 - Measured RMS Pressure Fluctuations at P_{10} with Oscillating Amplitude of 2.1 Degrees and $R_{nc} = 1.6 \times 10^6$	11
17 - Measured RMS Pressure Fluctuations at P_{10} with Oscillating Amplitude of 2.1 Degrees and $R_{nc} = 1.2 \times 10^6$	11

	Page
18 - Chordwise Location of Transition and Laminar Separation Versus α and R_{nc}	11
19 - Measured RMS Pressure Fluctuations at P_{10} with Three Reynolds Numbers and Oscillating Amplitude of 0.97 Degrees ($f = 10$ Hz).	12
20 - Measured RMS Pressure Fluctuations at P_{25} with Oscillating Amplitude of 2.1 Degrees and $R_{nc} = 1.6 \times 10^6$	12
21 - Measured RMS Pressure Fluctuations at P_{25} with Oscillating Amplitude of 2.1 Degrees and $R_{nc} = 1.2 \times 10^6$	12
22 - Measured RMS Pressure Fluctuations at P_{25} with Three Reynolds Numbers and Oscillating Amplitude of 0.97 Degrees ($f = 10$ Hz).	13
23 - Dynamic Pressure Distributions with $\alpha = 3.25 + 1.57 \sin \omega t$	14
24 - Comparison of Dynamic and Static Pressure Distributions at $\alpha = 4.0$ Degrees.	15
25 - Influence of V_∞ and Reduced Frequency on Relative Sound Power for $\alpha = 3.25 + 0.95 \sin \omega t$	16
26 - Cavitation Noise Signals $\sqrt{P^2}$ and Foil Angles for Runs 1411 and 1416, $\alpha = 3.25 + 0.95 \sin \omega t$	17
27 - Relative Sound Power $\bar{P}^2(\alpha)$ as a Function of Foil Angle for Runs 1411 to 1416 with σ_i , I_m & σ_d for Sheet Cavitation.	18
28 - Influence of V_∞ and Reduced Frequency on Relative Sound Power for $\alpha = 3.25 + 1.55 \sin \omega t$	18
29 - Cavitation Noise Signals $\sqrt{P^2}$ and Foil Angles for Runs 1401 and 1406, $\alpha = 3.25 + 1.55 \sin \omega t$	18
30 - Relative Sound Power $\bar{P}^2(\alpha)$ as a Function of Foil Angle for Runs 1401 and 1406	18
31 - Measured Maximum Cavity Length vs. Reduced Frequency	19
32 - Measured Foil Angles at Maximum Lift, Maximum Cavity Length, Noise Peak and Leading Edge Sheet Cavity Desinence for Runs 1401 to 1406.	19

	Page
33 - Relative Sound Pressure \bar{P}^2 Over One Cycle for a Continuously Cavitating Hydrofoil	19
34 - Cavitation Noise Signals $\sqrt{P^2}$ and Foil Angles for Runs 1510 and 1515, $\alpha = 3.25 + 0.32 \sin \omega t$	19

LIST OF TABLES

1 - Root-Mean-Square Boundary Layer Pressure Fluctuations at 25 Percent Chord (P_{25}) and 10 Percent Chord (P_{10})	6
2 - Dynamic Pressure Coefficient $C_{pu}(t)$	14
3 - Test Run Numbers and Associated Parameters	17

ABSTRACT

Significant effects of boundary layer characteristics on cavitation and the effect of unsteady cavitation on noise have been widely observed experimentally. In order to better understand these effects, an experiment with a two-dimensional hydrofoil, under sinusoidal pitching oscillation, was conducted in the 36-inch water tunnel at DTNSRDC. Three pin-hole-type pressure transducers were installed on the foil surface to measure pressure fluctuations and a hydrophone was used to measure the radiated cavitation noise. Two subjects are discussed in this paper: 1) relationship of boundary layer transition and pressure fluctuations with the hydrofoil in oscillation, and 2) noise generated by unsteady cavitation.

The magnitudes of pressure fluctuations in transition and turbulent regions are found to be independent of oscillation amplitude and frequency. However, the development of boundary layer and occurrence of transition are delayed with an increase in oscillation frequency. The influence of hydrofoil oscillation on cavitation inception is also discussed. With the occurrence of leading edge sheet cavitation, a significant effect of foil oscillation on cavitation noise is measured. At high reduced frequencies, extensive cloud cavitation is formed during the final phase of sheet cavity collapse and the noise level is significantly increased.

PREFACE

An earlier paper by the present authors at the 12th ONR symposium dealt with two subjects, the inception of cavitation on a two-dimensional foil and the physics of leading-edge sheet cavity stability and subsequent formation of cloud cavitation. The method developed to predict inception was based on Giesing's unsteady airfoil theory and assumed that viscous effects were of secondary importance. The present paper will explore the importance of the boundary layer development. In addition, as a continuation of the early study of cavitation instability, the importance of cloud cavitation in producing acoustic noise will be presented.

1. INTRODUCTION

Cavitation frequently is unavoidable on the lifting surfaces of hydrofoils and marine propellers. For many years, scientists and engineers have dealt with the problems of cavitation-induced noise, structural vibration and erosion associated with the operation of marine vehicles and hydraulic equipment. All three problems are related to the inception, growth, and collapse of vapor cavities.¹

Inception of cavitation in a fluid is the condition under which cavitation is first detected, either visually or acoustically. It had often been assumed that when making analytical predictions, cavitation inception occurs immediately after the static pressure on the body surface becomes equal to or less than the vapor pressure of the fluid. A research model, the International Towing Tank Conference (ITTC) headform, tested in different cavitation facilities demonstrates that cavitation inception on a given model can have many different physical forms and cavitation inception indices, depending on the environment and body surface condition.^{2,3} Departures of cavitation inception from the traditional rule are attributed to so-called "scale effects." The influence of boundary layer pressure fluctuations on cavitation inception is known to be one of the major sources of scale effect.^{2,4}

Rouse⁵ showed that the high pressure fluctuations generated in the turbulent shear layer of a free-jet can produce cavitation at static pressures which are higher than vapor pressure. Daily and Johnson⁶ showed that pressure fluctuations in the middle of a fully established turbulent boundary layer can initiate inception. Levkovskii and Chalov⁷ reported that turbulence in flow past a wing causes cavitation to inception earlier. Recent work by Arakeri and Acosta^{8,9} and Huang⁴ indicates that for supercritical Reynolds numbers for which bodies do not have laminar boundary layer separation, cavitation inception takes place in the region of transition from laminar to turbulent flow. For subcritical Reynolds numbers, cavitation inception is found to occur in the reattachment region following laminar boundary layer separation.

Significant boundary layer pressure fluctuations on body surfaces have been measured by Huang and Hannan¹⁰ and by Arakeri¹¹ in the reattachment region following laminar separation. In addition, Huang and Hannan reported that measured pressure fluctuations in a natural transition region are higher than fluctuations in a fully established turbulent boundary layer flow by a factor ranging from 2 to 3. Huang and Peterson¹² reported that a significant scale effect on cavitation inception induced by boundary layer pressure fluctuations exists between full-scale and model propellers due to large differences in Reynolds numbers.

The properties of the wall fluctuating pressure field associated with the growth of turbulent spots in a transition boundary layer on a flat plate have been measured by DeMetz et al.,¹³ DeMetz and Casarella,¹⁴ and Gedney.¹⁵ Each reported that pressure fluctuations in the transition region are smaller than those in the fully developed turbulent region. This result is not in agreement with the measurements of Huang and Hannan.¹⁰

A basic question has been raised as to whether the boundary layer pressure fluctuations in a natural transition region can be greater than those in a fully established turbulent boundary layer region. The significance of this point is that if the pressure fluctuations at transition are greater than in the fully developed turbulent boundary layer, then one can expect cavitation to preferentially occur at the transition location. In view of the significance of this question in cavitation scaling, fluctuating pressure measurements for a two-dimensional hydrofoil are given in this paper.

When a hydrofoil operates in waves or a propeller operates behind a ship hull, the lifting surfaces are subjected to temporally and/or spatially varying velocity and pressure fields. The time varying pressure field can be expected to have a significant effect on the characteristics of cavitation inception, growth, and collapse. As a first approximation, the unsteady effect on cavitation has been studied with oscillating hydrofoils by Miyata et al.,¹⁶ Radhi,¹⁷ Bark and van Berlekom,¹⁸ Shen and Peterson,¹⁹ and van Houten.²⁰ The hydrofoil approach is especially attractive for simulating a propeller blade operating behind an inclined shaft with the effective angle of attack oscillating periodically during each cycle of rotation. Available data demonstrate that the cavitation-inception angle-of-attack at the leading edge is different from inception angles determined from quasi-steady analysis based on uniform flow experiments.

Shen and Peterson¹⁹ showed that the computed potential-flow pressure distributions are subject to a significant phase shift with respect to the foil oscillation angle, which in turn influences the occurrence of cavitation inception. As previously mentioned, significant physical effects of boundary layer characteristics on cavitation have been well

documented. So far most transition and boundary layer pressure fluctuation studies have been limited to flat plates and headforms. In the first part of this paper the influence of oscillation on transition boundary-layer pressure fluctuations, and the possible effect of oscillation on cavitation inception for a two-dimensional hydrofoil, will be presented. As pointed out previously, cavitation frequently is unavoidable on the lifting surfaces of hydrofoils and marine propellers. In the second part of this paper the influence of oscillation on foil cavitation instability and noise will be presented.

2. EXPERIMENTAL APPARATUS AND TEST PROCEDURE

2.1 Foil and Instrumentation

A foil was machined from 17-4 PH stainless steel in the form of a rectangular wing of Joukowski section with the trailing edge modified to eliminate the cusp. The offsets are given by the following equation:

$$\begin{aligned} y/c &= 0.04077 \sin \theta - 0.02039 \sin (2\theta) & 0 \leq x/c \leq 0.7945 \\ \theta &= \cos^{-1} (1.888 x/c - 1) \\ y/c &= 0.08590 (1 - x/c) & 0.7945 \leq x/c \leq 1.0 \end{aligned} \quad (1)$$

To simulate prototype viscous effects at the leading edge as closely as possible, the model was designed with a chord length c of 24.1 cm, a span of 77.5 cm and a relatively large leading-edge radius. The maximum thickness to chord ratio is 10.5 percent. The foil surface was hand finished within $0.38 \mu\text{m}$ rms surface smoothness.

Pressure transducers were installed at a distance of 7.96, 24.1 and 60.3 mm from the leading edge. These locations correspond to 3.3, 10, and 25 percent of chord length from the leading edge. Kulite semiconductor pressure gages of the diaphragm type (Model number LQM-10-250-305) were mounted within a Helmholtz chamber connected to the foil surface by a pinhole. This arrangement permitted measurement of unsteady surface pressures due to foil oscillation and high frequency pressure fluctuations inside the boundary layer over a pressure range of $\pm 207 \text{ KPa}$ ($\pm 30 \text{ PSI}$). In order to increase the spatial resolution in measuring the local pressure fluctuations inside the boundary layer, the diameter of the pinholes installed on the foil surface was kept at 0.31 mm (0.012 inches). This arrangement also reduces the danger of cavitation damage to the pressure transducers. Extreme care was taken to fill the Helmholtz-type chamber through the pinhole under vacuum with deaerated water to minimize the possible occurrence of an air bubble trapped inside the chamber. A flat pressure response was observed up to 2,000 Hz in dynamic calibration tests. The calibration procedure used here was developed by the National Bureau of Standards,²¹ modified to the extent that water, rather than silicone oil, was the fluid medium. Since it was very important to determine the relative phase difference between the foil angle and the pressure gage signals, all amplification and recording equipment was selected to minimize the introduction of unwanted phase shifts.

The cavitation noise was sensed by a flush mounted hydrophone 117 cm downstream from the foil axis, on the top of the water tunnel's close-jet test section. The hydrophone was uncalibrated, so all noise measurements are relative to an arbitrary level.

2.2 Test Section

The closed-jet test section of the 36-inch water tunnel was modified by the insertion of sidewall liners to provide two flat sides. On each end of the foil a disc was attached. This disc rotated in a sidewall recess; thus the foil could be rotated without gap cavitation occurring between the end of the foil and the sidewall of the tunnel. One sidewall assembly was fitted with clear plastic windows to permit side view photography.

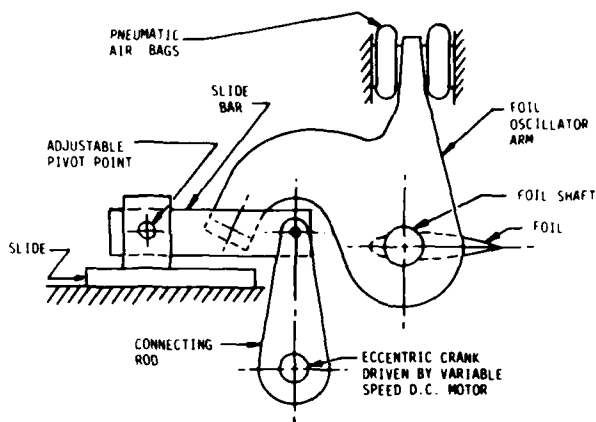


Figure 1 — Conceptual Design of Foil Oscillation Mechanism

The foil was oscillated in pitching motion around the quarter chord by a mechanism whose conceptual design is shown in Figure 1. With this type of design, the foil mean angle (α_0) can be adjusted statically and the amplitude of foil oscillation (α_1) can be continuously adjusted between 0° to 4° while in operation. The oscillation frequencies cover the range between 4 Hz to 25 Hz. Air bags were installed to reduce the fluctuating torque requirements on the motor drive system.

2.3 Data Reduction

Due to installation of two sidewall liners in the test section, the tunnel speed was corrected according to the area-ratio rule. The tape-recorded time histories of foil angle and pressures were digitized by using a Hewlett Packard 2100 minicomputer and reduced by using algorithms implemented on the DTNSRDC CDC-6000 digital computer. The time histories were recorded on one inch magnetic tape at 15 inches per second (38 cm/s) using IRIG standard intermediate band frequency modulation techniques. During digitization, pressure fluctuation data were filtered using four-pole Butterworth bandpass filters that have a -3 dB signal attenuation at 80 and 2,000 Hz for boundary layer pressure fluctuations. The run lengths used in the data reduction were nominally 40 seconds. For the oscillating foil data, the computer output consisted of values of mean and standard deviations of pressure fluctuations.

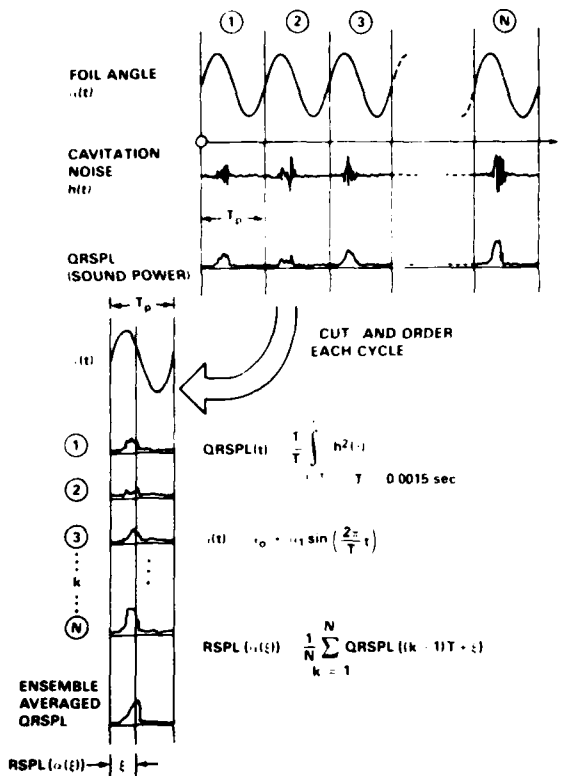


Figure 2 — Sequence of Ensemble Averaging
(From an unpublished report by R. Pierce, DTNSRDC)

The hydrophone signal was first bandpass filtered between 10 kHz and 40 kHz to minimize signal contamination from noncavitation related sources. This signal was then squared and passed through an averaging filter to obtain a "running average," i.e. quasi-stationary sound power levels, $\overline{p^2}$ as shown in Figure 2. This sound power level is also digitized along with the signals corresponding to the foil angle-of-attack and the mean foil angle. In order to obtain the average relative sound power, the digitized signal is averaged over the whole run. In order to determine the average waveform of the hydrophone signal during one cycle, a cycle is defined as being initiated and terminated when the increasing foil angle passes through its mean position. Each cycle is divided into $(1600/f)$ time increments, i.e. at a $f = 4$ Hz oscillation frequency, 400 time increments are used. The digitized hydrophone signal in each time increment is averaged over all of the cycles in a run. The averages in each of the increments then collectively represent the average waveform occurring for one cycle.

3. BOUNDARY LAYER PRESSURE FLUCTUATIONS ON A STATIONARY FOIL

Consider a steady uniform flow past a two-dimensional hydrofoil. Let the local pressure p on the foil surface be expressed in the following way:

$$p = p_i + \Delta p_i \quad (2)$$

where p_i is the mean pressure and Δp_i is the pressure associated with the boundary layer pressure fluctuations. Let C_{pi} denote local pressure coefficient:

$$C_{pi} = \frac{p - p_\infty}{\frac{1}{2} \rho V_\infty^2} = C_{pi_0} + \Delta C_{pi} \quad (3)$$

where

$$C_{pi_0} = \frac{p_i - p_\infty}{\frac{1}{2} \rho V_\infty^2} \quad (4)$$

and

$$\Delta C_{pi} = \frac{\Delta p_i}{\frac{1}{2} \rho V_\infty^2} \quad (5)$$

here ρ , p_∞ , and V_∞ are fluid density, reference free-stream static pressure and reference free-stream velocity, respectively.

3.1 Laminar Boundary Layer Stability Calculations

Let $k = \frac{\omega c}{2V_\infty}$ denote the reduced frequency where ω is the circular frequency associated with foil oscillation. The limiting case $k = 0$ corresponds to a stationary condition. A uniform flow past a stationary foil at an angle-of-attack α of 3.25 degrees will be considered first. The computed steady potential flow pressure distribution for this foil angle is shown in Figure 3. The flow field to be measured by the pressure gages at 3.3, 10 and 25 percent chord length is seen to be in a strong adverse pressure gradient. This fact will be shown to have a significant effect on the magnitude of boundary layer pressure fluctuations. The prediction of laminar boundary layer separation is based on the criterion of zero shear stress. The Smith disturbance amplification method²² is used to correlate and predict flow transition.

Let A/A_0 denote the Smith cumulative spatial amplification ratio A to its amplitude A_0 at the point of neutral stability. Let R_{nc} denote the Reynolds number based on chord length. As a numerical example, the computed amplification ratio versus chordwise location x/c is given in Figure 4a at

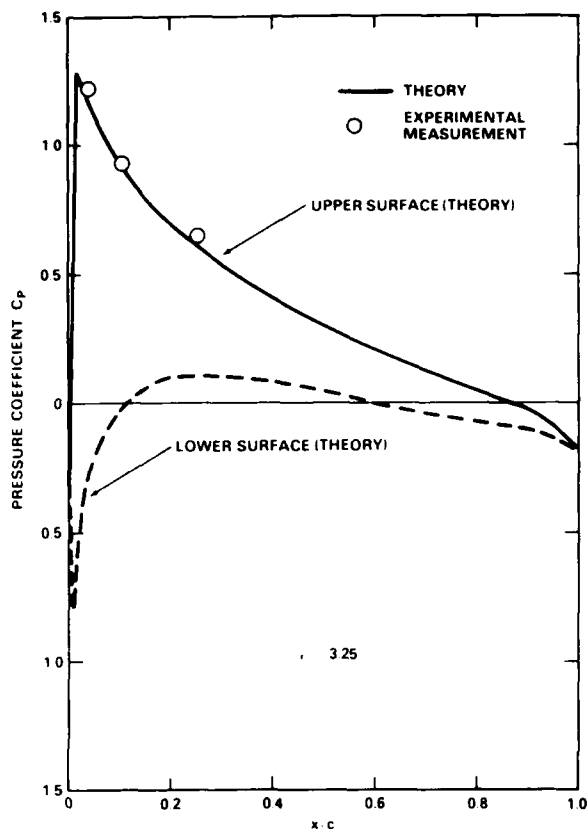


Figure 3 — Measured and Predicted Pressure Distributions

$R_{nc} = 1.6 \times 10^6$. The Smith cumulative spatial amplification ratio was computed for a range of nondimensional boundary layer disturbance frequencies $\bar{\Omega}$,

$$\bar{\Omega} = \frac{\Omega v}{V_{\infty}^2} \quad (6)$$

where Ω is the dimensional disturbance frequency. Figure 4a shows that disturbances will be significantly amplified in the frequency range of $\bar{\Omega} = 1.7 \times 10^{-4}$ to 3.2×10^{-4} which correspond to dimensional frequencies of 1,250 Hz to 2,350 Hz. Figure 4a also indicates that the frequency $\bar{\Omega} = 3.2 \times 10^{-4}$ has the largest amplification ratio up to $x/c = 0.11$. The free-stream velocity used in these computations is $V_{\infty} = 6.71$ m/s. The same method was used for stability calculations at other Reynolds numbers. The computed results are summarized in Figure 4b.

3.2 Experimental Results

The experiments with the foil at $\alpha = 3.25$ degrees were performed in the DTNSRDC 36-inch water tunnel. As seen in Figure 3, the measurements of static pressure coefficients are in good agreement with prediction. At speeds of 4.88, 6.71, 9.75, 13.11 and 14.94 meter/sec, the pressure responses measured at three foil locations are given in Figures 5a to 5e. The pressure gages located at 3.3, 10 and 25 percent chord lengths on the upper surface are denoted by P_3 , P_{10} and P_{25} , respectively. The purpose of steady runs was

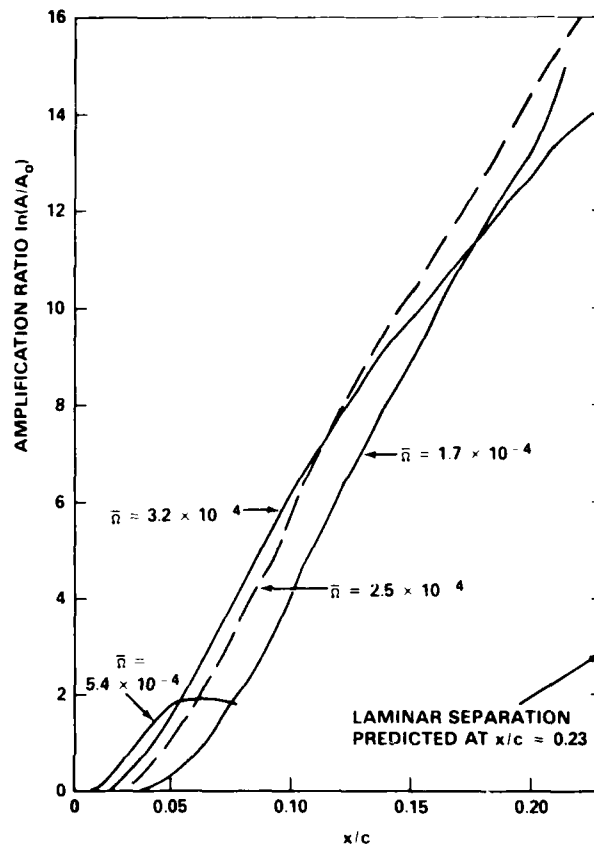


Figure 4a — Computed Amplification Ratios at Foil Angle $\alpha = 3.25$ deg and $R_{nc} = 1.6 \times 10^6$

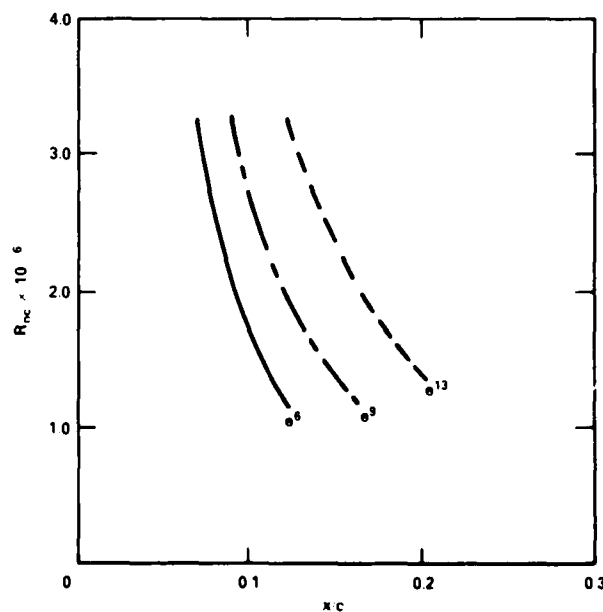


Figure 4b — Effect of Reynolds Numbers on Amplification Ratios at $\alpha = 3.25$ deg

to provide reference data to be used for comparison with dynamic runs. Consequently, the test runs given in Figures 5a to 5e were conducted with the oscillating mechanism in motion and the oscillating amplitude α_1 set to zero to incorporate the possible effect of noise and vibration on the measured phenomena.

RUN NO. 7001

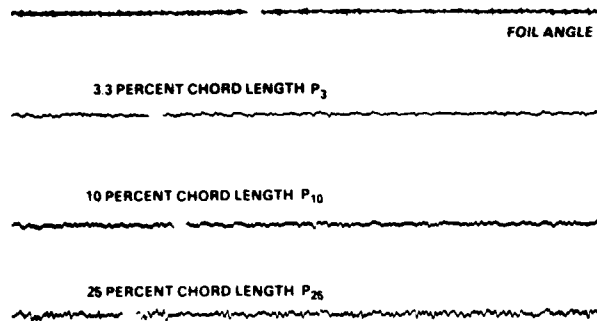


Figure 5a — Measured Pressure Fluctuations at $R_{nc} = 1.2 \times 10^6$ in a Steady Flow at $\alpha = 3.25$

RUN NO. 8028

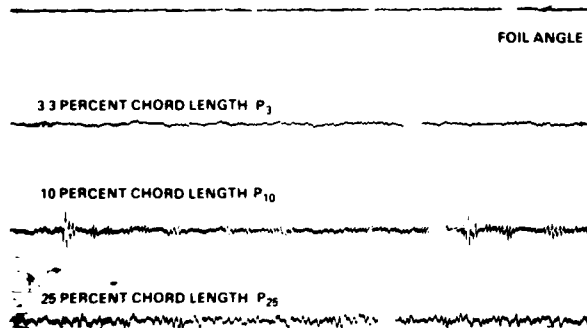


Figure 5b — Measured Pressure Fluctuations at $R_{nc} = 1.6 \times 10^6$ in a Steady Flow at $\alpha = 3.25$

RUN NO. 8040

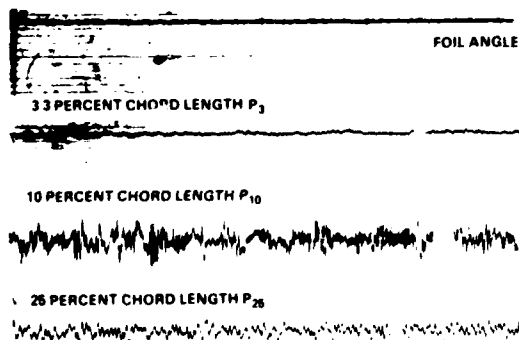


Figure 5c — Measured Pressure Fluctuations at $R_{nc} = 2.4 \times 10^6$ in a Steady Flow at $\alpha = 3.25$

RUN NO. 8044

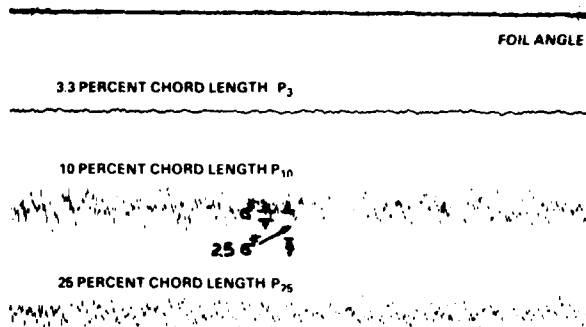


Figure 5d — Measured Pressure Fluctuations at $R_{nc} = 3.2 \times 10^6$ in a Steady Flow at $\alpha = 3.25$

RUN NO. 8056

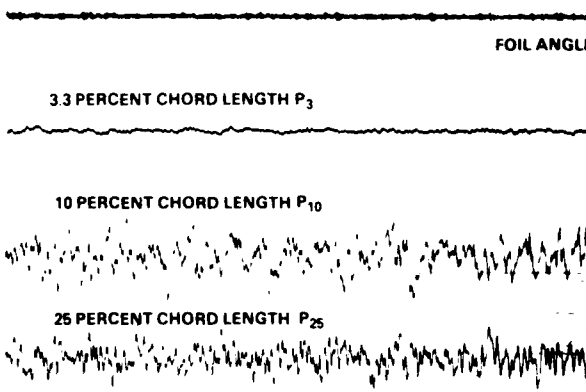


Figure 5e — Measured Pressure Fluctuations at $R_{nc} = 3.6 \times 10^6$ in a Steady Flow at $\alpha = 3.25$

The energy spectrum based on narrow band frequency analysis from 80 to 5040 Hz of Run 8028 at pressure gage P_{10} is given in Figure 6. The maximum fluctuating signal at P_{10} corresponds to 2650 Hz. This value is in close agreement with the computed frequency of the most unstable disturbances; see Figure 4a. The energy spectra of pressure responses based on narrow band frequency analysis were conducted for several test Runs. Figure 6 shows a sharp peak at 4.7 kHz at pressure gage P_{10} . The same kind of sharp peak at 4.7 kHz was observed in all the runs analyzed. A similar phenomenon was observed at 5.0 kHz at pressure gage P_{25} . It is suspected that this may be resonance phenomenon associated with pinhole-type pressure gages. The pressure gages had been dynamically calibrated up to 2,000 Hz with flat response. Consequently, the data given in Figures 5a to 5e were bandpass filtered with 4 pole Butterworth filters from 80 to 2,000 Hz. Burton²³ has shown that the energy spectrum of a flow field in an adverse pressure gradient is compacted in a much narrower and lower frequency ranges than the energy spectrum associated with a flow field in a zero pressure gradient.

A comparison of pressure response measurements and stability calculations suggests that the boundary layer at P_{25} (25 percent chord length) for all the runs given in Figure 5a to 5e is fully turbulent. The measured root-mean-square (rms) pressure fluctuations normalized by the free-stream dynamic

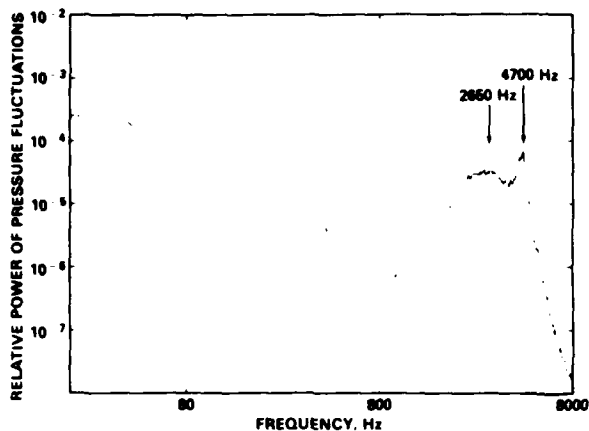


Figure 6 — Energy Spectrum of Run 8028 at $R_{nc} = 1.6 \times 10^6$

head are given in Table 1. The values of ΔC_{pt} range between 0.0065 to 0.011. Burton reported that the measured rms pressure fluctuation coefficient normalized by the free-stream dynamic head is measurably smaller in an adverse pressure gradient (around 0.0078) than in a favorable pressure gradient (around 0.010). Huang and Hannan¹⁰ measured 0.015 on an axisymmetric body. The present data were digitized through a bandpass filter from 80 to 2,000 Hz. The loss of high frequency range may influence the resolutions of pressure gage measurements and underestimate the magnitude of pressure fluctuations.

RUN NO	V, m/s	$R_{nc} \times 10^6$	ΔC_{pt} at P_{25}		ΔC_{pt} at P_{10}	
7001	4.88	1.2	0.0125	0.0113	0.0006	0.0002
8028	6.71	1.6	0.0097	0.0092	0.0117	0.0111
8040	9.75	2.4	0.0076	0.0074	0.0137	0.0136
8044	13.11	3.2	0.0085	0.0085	0.0095	0.0095
8056	14.98	3.6	0.0085	0.0085	0.0092	0.0092

*NOISE SIGNAL SUBTRACTED

TABLE 1 — ROOT-MEAN-SQUARE BOUNDARY LAYER PRESSURE FLUCTUATIONS AT 25 PERCENT CHORD (P_{25}) AND 10 PERCENT CHORD (P_{10})

Additionally, Table 1 shows that at a given location the measured pressure fluctuation coefficients decrease with an increase in speed. The same trend was also reported by Burton. Measurements by Ludwig and Tillman²⁴ showed that the shearing stress in a turbulent boundary layer decreased significantly with an increase in momentum thickness Reynolds number. Blake²⁵ reported that the shear stress rather than the free-stream dynamic head should be used to collapse the data. All these findings suggest that the boundary-layer pressure fluctuation coefficient to be used for model/full-scale cavitation scaling is not a universal constant, as used in Reference 12, but instead is a function of Reynolds number.

Stability calculations at $R_{nc} = 1.6 \times 10^6$ show that amplification ratios of e^6 , e^9 and e^{11} are reached at $x/c = 0.10$, 0.13 and 0.16, respectively. Laminar separation is predicted to occur at $x/c = 0.23$. Theoretical computations suggest that natural transition from laminar to turbulent boundary layers is to be expected to occur upstream of the laminar separation point at this Reynolds number. Thus, natural transition precludes the possibility of laminar separation.

At a speed of 4.88 m/s, Figure 5a shows that the flow at 3.3 and 10 percent chord lengths are laminar. With an increase in speed to 6.71 m/s, corresponding to $R_{nc} = 1.6 \times 10^6$, a strong pressure fluctuating signal with intermittency is noticed at 10 percent chord; see Figure 5b. The bursting signal observed in Figure 5b is related to natural transition. It was found that the computed amplification ratio of e^6 correlated well with the measured location of natural transition for the present experimental setup at $R_{nc} = 1.6 \times 10^6$. For other Reynolds numbers the computed locations of the amplification ratios of e^6 were used to indicate the start of natural transition.

At a speed of 9.75 m/s, corresponding to $R_{nc} = 2.4 \times 10^6$, the stability calculations predict an amplification ratio of $e^{8.5}$ at P_{10} . Measured pressure responses suggest that the flow at 10 percent chord is in the final phase of transition with an intermittency factor close to unity; see Figure 5c. The rms pressure fluctuations normalized by the free-stream dynamic head, are given in Table 1. The measured rms pressure fluctuation at 10 percent chord in the transition region are seen to be greater than those measured at 25 percent chord in the turbulent region. This observation is based on data analysis with a bandpass filter of 80 to 2,000 Hz. In the few cases when the bandpass filter upper limit increased to 5,040 Hz, the same conclusion held.

The properties of the wall fluctuating pressure field associated with the growth of turbulent spots in a natural transition boundary layer on a flat plate have been measured by DeMetz et al.,¹³ DeMetz and Casarella,¹⁴ and Gednev.¹⁵ They all report that the pressure amplitudes in the wall pressure field of individual spots are approximately equal to those in the fully turbulent boundary layer region. As the intermittency factor γ increases, the power spectral densities increase systematically to a maximum value in the fully turbulent condition.¹³

$$p^2(\gamma) = \gamma p^2(\gamma), \quad (7)$$

These results suggest that the pressure fluctuations measured in a natural transition region are smaller than those in a turbulent region, which is not in agreement with the present measurements.

Pressure fluctuations in regions of natural flow transition on an axisymmetrical body were also measured by Huang and Hannan.¹⁰ Compared to the pressure fluctuations measured in a fully established turbulent region, the intensity of pressure fluctuations in the transition region is higher than in the turbulent region. The present results agree with the results of Huang and Hannan. These measurements and the present measurements were made in flows with adverse pressure gradients, whereas the linear relationship given in Equation (7) is derived from measurements on a flat plate with zero pressure gradient. It is suspected that the cause of differences in the two sets of data is differences in the pressure gradients. This difference is further amplified in the following series of tests. The pressure fluctuations at a speed of 13.11 m/s, corresponding to $R_{nc} = 3.2 \times 10^6$, are given in Figure

5d. This figure suggests that the flow is turbulent at 10 percent chord; this correlates with the stability calculations which indicated that the amplification ratio reached about e^9 to e^{10} at P_{10} . Figure 5d also suggests that the location of transition has moved ahead of P_{10} . The measured pressure coefficient at this speed is smaller than the one measured at a speed of 9.75 m/s. This fact seems to support the argument that the pressure fluctuation in a transition region is greater than in a turbulent region with an adverse pressure gradient. A further increase in speed to 14.94 m/s reduces the pressure fluctuation further as shown in Figure 5e.

As a final remark, Figure 5d shows that the frequently-occurring large negative pressure fluctuations are approximately 2.5 times higher than their rms value in the transition region at P_{10} and 2.0 times higher than their rms value in the fully established turbulent region at P_{25} . These results are in close agreement with the Huang and Hannan measurements.¹⁰ Huang and Peterson¹² suggested that the frequently-occurring large negative pressure fluctuations in transition may be responsible for cavitation inception events.

4. BOUNDARY LAYER PRESSURE FLUCTUATIONS WITH FOIL IN OSCILLATION

4.1 The Oscillating Foil

The foil oscillates sinusoidally in pitching motion around the quarter chord point, measured from the foil leading edge. The instantaneous foil angle is denoted by:

$$\alpha = \alpha_0 + \alpha_1 \sin(\omega t) \quad (8)$$

where α_0 , α_1 , and ω are the mean foil angle, amplitude of foil oscillation and oscillation frequency, respectively. Let ϕ denote the phase angle between the pressure response and the instantaneous foil angle. At a given location on the foil, the time dependent local pressure and pressure coefficient are expressed by:

$$P(t) = P_s + |P_u| \sin(\omega t + \phi) + \Delta P_t$$

$$C_p(t) = C_{ps} + |\Delta C_{pu}| \sin(\omega t + \phi) + \Delta C_{pt}$$

where

$$C_{ps} = \frac{P_s - P_\infty}{\frac{1}{2} \rho V_\infty^2} \quad (9)$$

$$|\Delta C_{pu}| = \frac{|P_u|}{\frac{1}{2} \rho V_\infty^2}$$

$$\Delta C_{pt} = \frac{\Delta P_t}{\frac{1}{2} \rho V_\infty^2}$$

Here, C_{ps} , $|\Delta C_{pu}|$ and ΔC_{pt} respectively denote mean potential flow pressure coefficient, dynamic potential flow pressure coefficient, and the unsteady pressure coefficient associated with boundary layer pressure fluctuations. The objective of the work described here was to determine the influence of foil oscillation on transition and magnitudes of boundary layer pressure fluctuations.

4.2 Flow Description

For a typical propeller operating behind an inclined shaft, the lifting surface representing a propeller blade will encounter a periodic pressure field. The amplitude of pressure fluctuation depends on the ship speed and the angle of inclination. Angle-of-attack variations of 0.5 to 2.0 degrees at the 0.7 propeller radius are expected to represent a range of practical interest. The effect of unsteady angle-of-attack variations on lifting surface boundary-layer pressure fluctuations was investigated by pitching the previously-described two-dimensional hydrofoil sinusoidally.

A typical oscillograph plot of pressure responses with the foil in oscillation is shown in Figure 7. The data were bandpass filtered from 80 to 2,000 Hz. The low frequency periodic part has been subtracted. To accommodate an oscillation cycle of the foil on a reasonably sized sheet, the trace was processed at 2 inches per second paper speed. (Figures 5a to 5e were processed at 10 inches per second paper speed.) The first line from the top gives the instantaneous foil angle. In this example, the frequency of foil oscillation is 4 Hz. The instantaneous foil angle is given by $\alpha = 3.25^\circ + 2.1^\circ \sin \omega t$. The speed is 9.75 m/s, corresponding to $R_{nc} = 2.4 \times 10^6$. Recall that in the steady run ($\alpha = 3.25^\circ$) at $R_{nc} = 2.4 \times 10^6$ (Figure 5b), the flow was in the final stage of transition at the 10 percent chord length. The low amplitude unsteady signal appearing at 3.3 percent chord length is due to mechanical noise caused by the oscillator motion and the electrical noise within the recording electronics.

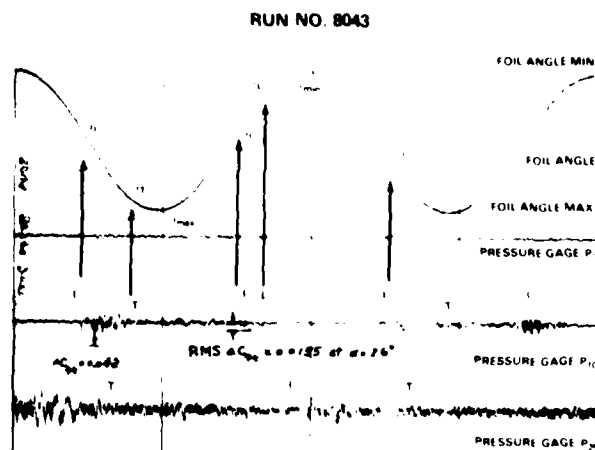


Figure 7 — Sample Oscillograph Record at $R_{nc} = 2.4 \times 10^6$, $f = 4$ Hz and $\alpha = 3.25 + 2.1 \sin \omega t$

In order to describe the observed change in transition location with foil angle, consider the pressure response at 25 percent chord length, P_{25} . Figure 7 suggests that the flow is turbulent and that the location of transition is ahead of P_{25} when the foil is at the maximum foil angle $\alpha = \alpha_{max}$. As the foil angle begins to decrease, the location of transition moves toward the trailing edge. At some intermediate foil angle $\alpha = \alpha_1$, the signals of pressure fluctuations are intensified and the

transition is assumed to occur at P_{25} . After the foil reaches $\alpha = \alpha_{min}$, the foil angle begins to increase and the movement of transition is reversed toward the leading edge. Finally, the flow at P_{25} becomes fully turbulent again at $\alpha = \alpha_T$.

Next, consider the pressure response at 10 percent chord length, P_{10} . In this example, the minimum foil angle is $\alpha_{min} = 1.15^\circ$. Figure 7 suggests that the flow is laminar at P_{10} when the foil angle is at α_{min} . The location of transition is aft of the 10 percent chord length. As the foil angle begins to increase, transition moves forward with instability occurring at a certain foil angle, $\alpha = \alpha_T$. A further increase in the foil angle produces full turbulence at $\alpha = \alpha_T$. It should be remarked that the pressures at P_{10} must be multiplied by a factor of 1.15 to account for difference in gage sensitivities if a direct comparison of pressure fluctuations between P_{25} and P_{10} are to be made on the oscillograph plot. The flow remains turbulent when the foil angle reaches $\alpha = \alpha_{max}$. This is followed by a decrease in foil angle. At $\alpha = \alpha_T$, flow transition occurs again at P_{10} . A further decrease in foil angle produces laminar flow at $\alpha = \alpha_L$. The rms pressures at P_{10} derived from Figure 7 are given in Figure 8. Figure 8 shows that the rms value of ΔC_{pt} attains the maximum of 0.0155 at the foil angle $\alpha = 2.6$ degrees. Figure 7 gives a measured large negative pressure fluctuations of $\Delta C_{pt} = 0.042$, which is approximately 2.7 times higher than the peak value (rms) shown in Figure 8. This result is in agreement with the previous stationary runs.

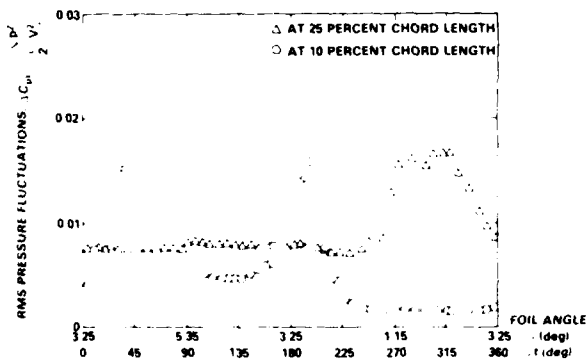


Figure 8 - Measured RMS Pressure Fluctuations on Run 8043 at $R_{nc} = 2.4 \times 10^6$ and $\alpha = 3.25 + 2.1 \sin \omega t$

4.3 Unsteady Effects

A series of dynamic runs was conducted to examine unsteady effects on boundary layer pressure fluctuations. A free-stream speed of $V_\infty = 9.75$ m/s was used for this series of experiments. The instantaneous foil angle α is given by $\alpha = 3.25 + \alpha_1 \sin \omega t$. The oscillation amplitude α_1 covered the range from 0 to 2.1 degrees. The oscillation frequency, $f = \omega/2\pi$, covered the range from 4 to 15 Hz. Due to the increased background noise, the pressure fluctuation associated with the 25 Hz foil oscillation are not presented here.

Recall the case $\alpha_1 = 0$, corresponding to Run 8040 as given in Figure 5c. The flow at P_3 (3.3 percent chord length) is seen to be laminar. The flow at P_{10} is seen to be in the final phase of transition. The flow at P_{25} is seen to be fully turbulent.

4.3.1 Pressure Fluctuations at 10 Percent Chord Length (P_{10})

The case with $\alpha_1 = 0.5$ degrees is considered first. It is remarked that the flow at 3.3 percent chord is laminar throughout the whole series of runs. Because the pressure fluctuations in dynamic runs are non-stationary, the test data were digitized to obtain a rms value (see Figure 2). The corresponding rms pressure fluctuations at P_{10} are shown in Figure 9 for oscillation frequencies of 4, 5.5 and 15 Hz. The vertical axis gives rms pressure fluctuations normalized by the free-stream dynamic head. The horizontal axis gives the instantaneous foil angle α and the oscillation angle ωt . The magnitudes of the pressure fluctuations are seen to vary with the instantaneous foil angles. Figures 5c and 9 suggest that the location of transition is slightly aft of P_{10} at $\alpha = 3.25$ degrees. As the foil angles are increased, transition moves forward toward P_{10} . The measured rms pressure fluctuations at P_{10} are systematically intensified. As the foil angle approaches 3.60 degrees, the location of transition occurs at P_{10} and the magnitude of pressure fluctuations attains a maximum. A further increase in foil angle moves the transition ahead of P_{10} ; and the magnitude of pressure fluctuations measured at P_{10} is reduced. After the foil angle reaches α_{max} the foil angle begins to decrease, transition moves downstream toward P_{10} and the intensity of pressure fluctuations measured at P_{10} increases again. At a foil angle of about 3.25 degrees ($\omega t = 180$ degrees), the location of transition approximately coincides with P_{10} . A further decrease in foil angle moves the transition location toward the trailing edge and the pressure fluctuations measured at P_{10} begin to decrease. Transition is seen to pass through P_{10} twice in every cycle of oscillation. This results in the appearance of two peaks in pressure fluctuations. The whole sequence of variation in pressure fluctuations with instantaneous foil angle can be best illustrated with large oscillation amplitudes.

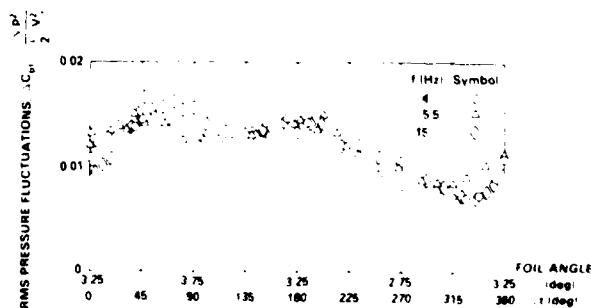


Figure 9 - Measured RMS Pressure Fluctuations at P_{10} with Oscillating Amplitude of 0.5 Degrees and $R_{nc} = 2.4 \times 10^6$

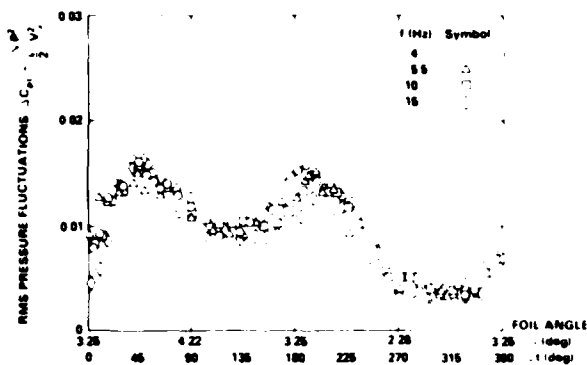


Figure 10 — Measured RMS Pressure Fluctuations at P_{10} with Oscillating Amplitude of 0.97 Degrees and $Re_c = 2.4 \times 10^6$

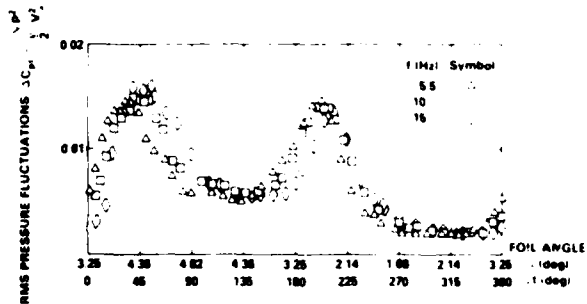


Figure 11 — Measured RMS Pressure Fluctuations at P_{10} with Oscillating Amplitude of 1.57 Degrees and $Re_c = 2.4 \times 10^6$

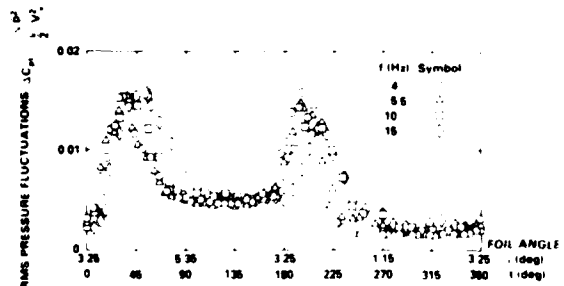


Figure 12 — Measured RMS Pressure Fluctuations at P_{10} with Oscillating Amplitude of 2.10 Degrees and $Re_c = 2.4 \times 10^6$

Figures 10, 11, and 12 give the rms pressure fluctuations measured at P_{10} for pitch oscillation amplitudes of 0.97, 1.57 and 2.10 degrees. The general patterns among these figures are similar. Based on this series of experiments, we can make the following observations concerning pressure fluctuations at the 10-percent chord location:

1. At the 10-percent point on the foil, there are two peaks of pressure fluctuations associated with advancing and receding transition locations during each cycle of oscillation. The magnitudes of the rms pressure amplitudes for both advancing and receding boundary layer transitions are the same at low values of oscillation frequency (4 and 5.5 Hz). However, at high values of oscillation frequency (10 and 15 Hz) the magnitude associated with advancing transition is generally greater than the magnitude of the receding transition.
2. The peak values of rms pressure fluctuations associated with advancing transition are seen to be independent of oscillation amplitudes and frequencies and they are almost the same with the values measured under steady conditions. These results provide a contrast between the boundary layer pressure fluctuations and unsteady potential flow pressure distributions. In the previous paper,¹⁷ we showed that the magnitudes of dynamic pressure responses of the potential flow (first harmonic) depend linearly on the oscillation amplitudes and vary significantly with oscillation frequencies.
3. In the previous paper,¹⁸ we were able to successfully correlate all of the data on the phase relationship between the peak of dynamic pressure response in the time-varying mean flow and the instantaneous foil angle by use of the reduced frequency parameter K . However, in the present paper, due to the scattering of the data, we can only qualitatively state that the locations of boundary layer transition are delayed with an increase in reduced frequency.
4. Consider pressure fluctuations in the region between $90 < \omega < 180$ degrees. It was stated previously that in this region, transition is located forward of P_{10} and that the magnitude of pressure fluctuations decreases systematically with increase of oscillation amplitude. Referring to Figure 12, for an oscillation amplitude $\alpha_1 = 2.10$ degrees, the fact that the pressure fluctuations remain at a constant value of $\Delta C_{pt} \approx 0.005$ for $90 < \omega < 180$, indicates that the flow is fully turbulent in this region. This value ($\Delta C_{pt} \approx 0.005$) measured at P_{10} is smaller than the value ($\Delta C_{pt} \approx 0.008$) measured at P_{25} with turbulent flows at both locations. It is not clear whether the magnitudes of adverse pressure gradients in these two locations control that difference.
5. Consider the flow characteristics in the region around $270 < \omega < 360$ degrees. It was stated previously that the transition point is located far aft of P_{10} . With an increase in amplitude of oscillation the flow becomes laminar again at P_{10} , as seen in Figures 11 and 12 where the ΔC_{pt} signal observed in the range $270 < \omega < 360$ may be attributed to noise contamination.

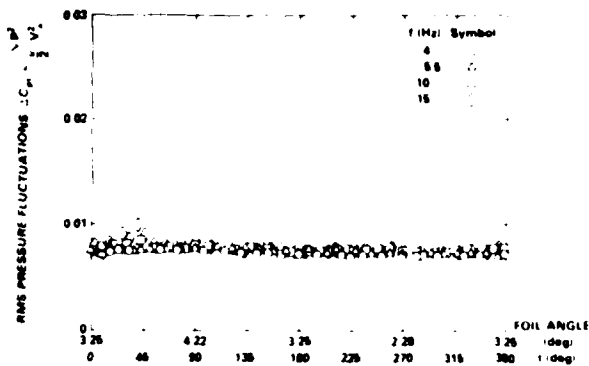


Figure 13 - Measured RMS Pressure Fluctuations at P_{25} with Oscillating Amplitude of 0.97 Degrees and $R_{nc} = 2.4 \times 10^6$

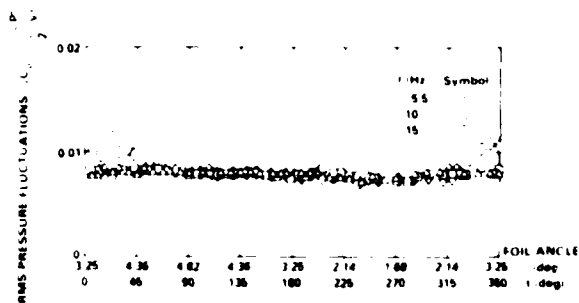


Figure 14 - Measured RMS Pressure Fluctuations at P_{25} with Oscillating Amplitude of 1.57 Degrees and $R_{nc} = 2.4 \times 10^6$

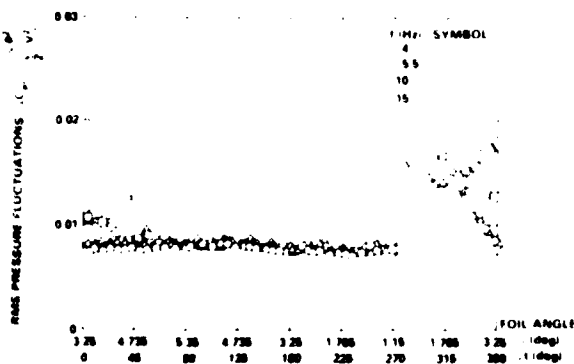


Figure 15 - Measured RMS Pressure Fluctuations at P_{25} with Oscillating Amplitude of 2.1 Degrees and $R_{nc} = 2.4 \times 10^6$

4.3.2 Pressure Fluctuations at 25 Percent Chord Length (P_{25})

Figures 13, 14, and 15 give rms pressure fluctuations at P_{25} for oscillating amplitudes of 0.97, 1.57, and 2.10 degrees, respectively. The flow at P_{25} is fully turbulent with $\alpha_1 = 0.5$ degrees (not shown in the figures) throughout each cycle of oscillation. Based on this series of experiments, we can make the following observations:

1. The value of rms pressure fluctuations in a fully established turbulent flow ($\Delta C_{pt} = 0.0080$) is independent of oscillating amplitudes and frequencies. This value is almost identical to the value measured in the steady runs.
2. With an increase in oscillation amplitude, transition moves toward P_{25} in the region $270 < \omega t < 360$. The magnitudes of pressure fluctuations are consequently intensified at P_{25} as seen in Figure 15. Simultaneously, the flow becomes laminar at P_{10} (see Figure 12). Consistent with the observation at P_{10} , the occurrence of peak pressure fluctuations at P_{25} is delayed by increasing the oscillation frequency.
3. The influence of advancing and receding transition points on pressure fluctuations measured at P_{25} is seen to be compatible with the behavior at P_{10} .
4. As shown in Figures 11 to 15 boundary-layer transition in an oscillating foil is delayed by an increase in oscillation frequency. It is further noticed that the pressure fluctuations in a transition region ($\Delta C_{pt} = 0.016$) are greater than in a fully turbulent region ($\Delta C_{pt} = 0.0080$), by a factor of 2. This result is in agreement with the observations in steady runs.

4.4 Reynolds Number Effects

Consider a local Reynolds number R_{nc} based on chord length at the 0.7 propeller radius. Because the local Reynolds number associated with a model propeller may vary from one test facility to another, additional dynamic runs were conducted to examine the effect of Reynolds number on boundary layer pressure fluctuations. These additional runs were made at R_{nc} values of 1.2×10^6 , 1.6×10^6 and 3.6×10^6 . The earlier runs, already discussed, were made at the R_{nc} values of 2.4×10^6 .

4.4.1 Pressure Fluctuations at 10-Percent Chord Length (P_{10})

Figures 16 and 17 give the rms pressure fluctuations measured at P_{10} for $R_{nc} = 1.6 \times 10^6$ and 1.2×10^6 , respectively. The examples given in these two figures are for an oscillation amplitude of $\alpha_1 = 2.10$ degrees. Once again, two peaks in pressure fluctuations associated with advancing and receding transition locations are observed for each cycle of oscillation. The magnitudes of these two peaks are markedly different. Additionally, the rms magnitudes associated with advancing transition are significantly intensified at the lowest value of $R_{nc} = 1.2 \times 10^6$, reaching as high as 10 percent of the dynamic head. The ordinate in Figure 17 has been modified to accommodate the significant increase in magnitude.

The values of cumulative spatial amplification ratio and locations of laminar separation computed for steady flow are shown in Figure 18. It was previously shown in steady runs that the bursting signal associated with natural transition in the present test set-up is best correlated with an amplification ratio of e^6 . The chordwise locations for disturbances to achieve amplification ratios of e^6 are shown in Figure 18 for three values of Reynolds number. Within the range of foil angles tested, laminar boundary-layer stability computations indicate that natural transition will occur earlier than laminar separation when $R_{nc} = 2.4 \times 10^6$. On the other hand, laminar separation will occur prior to natural transition at foil angles above 4.8 degrees at $R_{nc} = 1.6 \times 10^6$ and 4.2 degrees at $R_{nc} = 1.2 \times 10^6$.

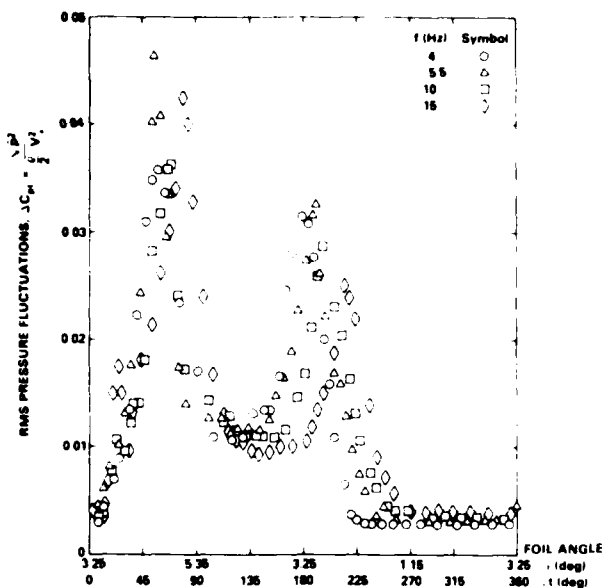


Figure 16 - Measured RMS Pressure Fluctuations at P_{10} with Oscillating Amplitude of 2.1 Degrees and $R_{nc} = 1.6 \times 10^6$

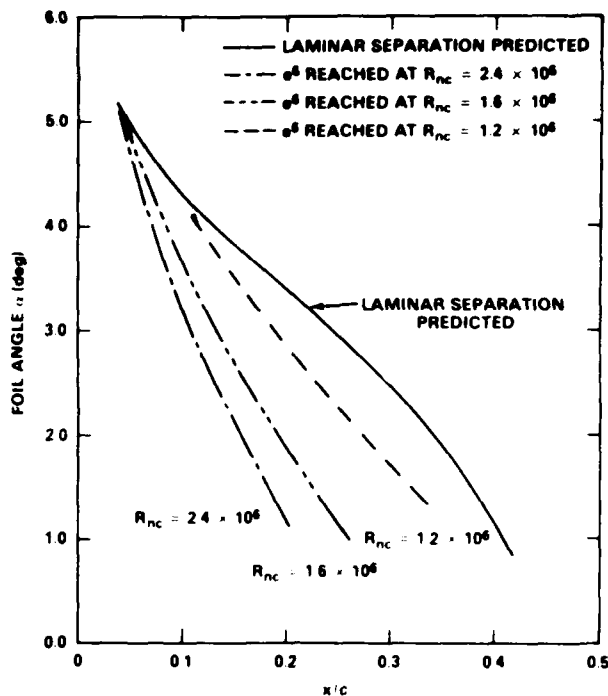


Figure 18 - Chordwise Location of Transition and Laminar Separation Versus α and R_{nc}

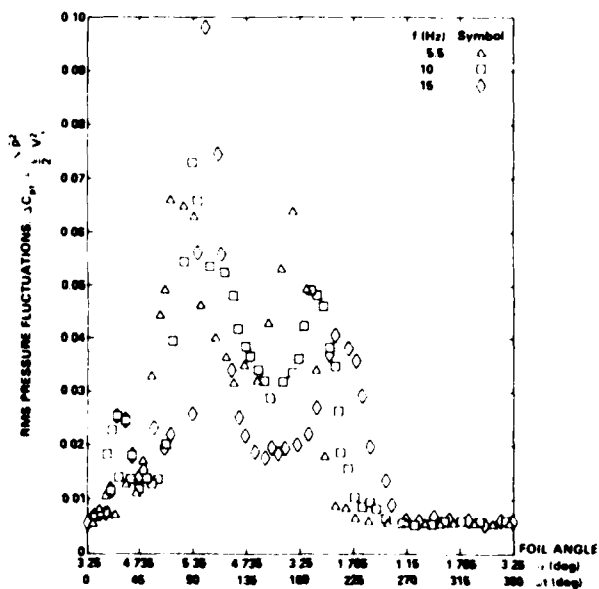


Figure 17 - Measured RMS Pressure Fluctuations at P_{10} with Oscillating Amplitude of 2.1 Degrees and $R_{nc} = 1.2 \times 10^6$

In comparison, Figure 12 shows the values of ΔC_{pt} at an oscillation amplitude of 2.1 degrees and $R_{nc} = 2.4 \times 10^6$. The maximum pressure fluctuations associated with advancing transition occur at about $\alpha = 4.5$ degrees for an oscillation frequency of 5.5 Hz. Figures 4 and 18 suggest that the maximum pressure fluctuations are related to a natural transition phenomenon. The rms pressure fluctuations due to advancing transition are $\Delta C_{pt} = 0.016$. On the other hand, at the lowest value of R_{nc} examined, $R_{nc} = 1.2 \times 10^6$, Figure 17 shows that the maximum pressure fluctuations occur at about 5.3 degrees at 5.5 Hz with rms pressure fluctuations reaching to $\Delta C_{pt} = 0.10$. Figure 18 suggests that this peak pressure is associated with laminar separation. The same discussion is applicable to Figure 16. The present result is in agreement with Huang and Hannan's finding that pressure fluctuations associated with laminar separation are much greater than for natural transition.

Figures 12, 16 and 17 show that the occurrence of advancing transition sets in earlier as Reynolds number increases. This trend is in agreement with the boundary layer stability calculations shown in Figure 4. To demonstrate this fact more clearly, the pressure fluctuations measured from three dynamic runs at $R_{nc} = 3.6 \times 10^6$, 2.4×10^6 and 1.2×10^6 are shown in Figure 19. The oscillation amplitude and fre-

quency associated with this example are 0.97 degrees and 10 Hz, respectively. For $R_{nc} = 1.2 \times 10^6$, peak pressure fluctuations never reaches P_{10} . Consequently, only one major peak pressure associated with laminar separation is noticed in the whole cycle of oscillation. In Figure 19 the associated background noise was corrected in such a way that ΔC_{pt} became zero in the laminar flow region. Due to the phase shift associated with the potential flow pressure distributions and the foil angles, the process of becoming laminar flow is achieved at a foil angle greater than α_{min} .

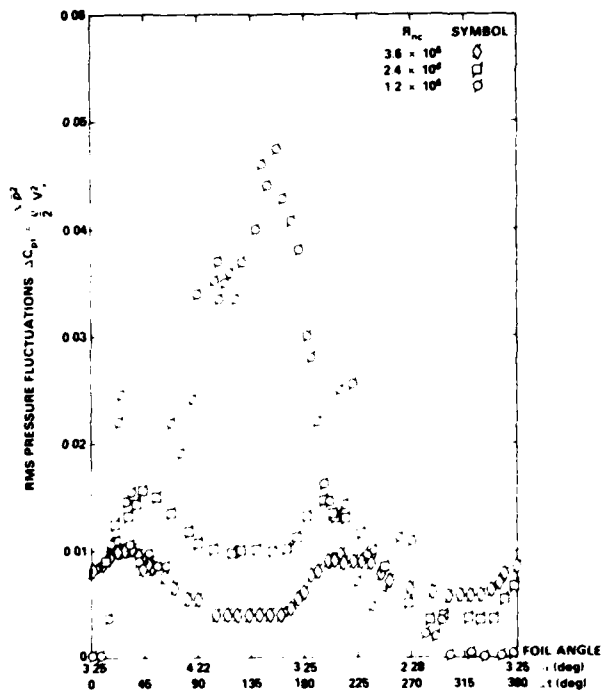


Figure 19 — Measured RMS Pressure Fluctuations at P_{10} with Three Reynolds Numbers and Oscillating Amplitude of 0.97 Degrees ($f = 10$ Hz)

4.4.2 Pressure Fluctuations at 25 Percent Chord Length (P_{25})

Figures 20 and 21 give rms pressure fluctuations measured at P_{25} for $R_{nc} = 1.6 \times 10^6$ and 1.2×10^6 , respectively. These two figures support the previous observation that ΔC_{pt} in a fully established turbulent region is independent of oscillation frequency. The same conclusion may be drawn from Figure 22. Additionally, the values of ΔC_{pt} are seen to increase with decreasing Reynolds numbers.

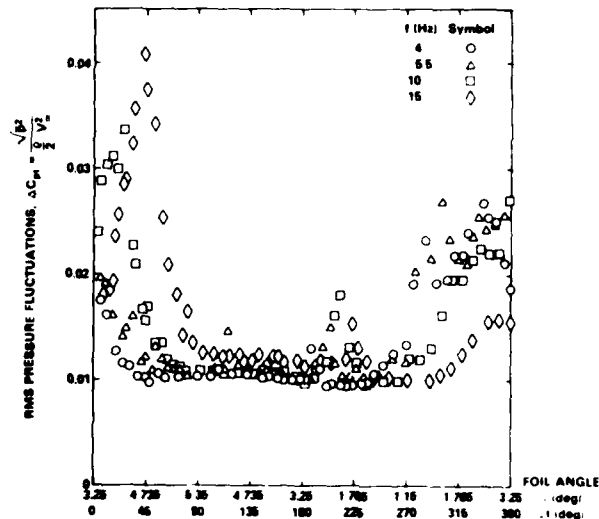


Figure 20 — Measured RMS Pressure Fluctuations at P_{25} with Oscillating Amplitude of 2.1 Degrees and $R_{nc} = 1.6 \times 10^6$

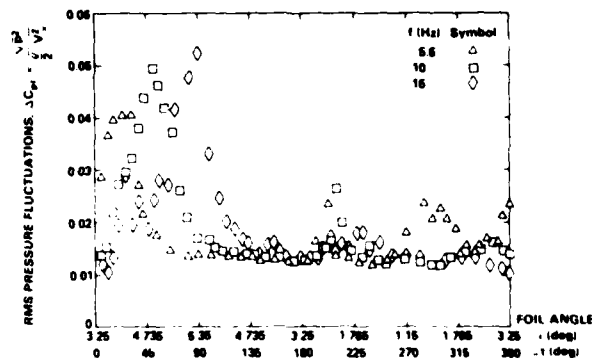


Figure 21 — Measured RMS Pressure Fluctuations at P_{25} with Oscillating Amplitude of 2.1 Degrees and $R_{nc} = 1.2 \times 10^6$

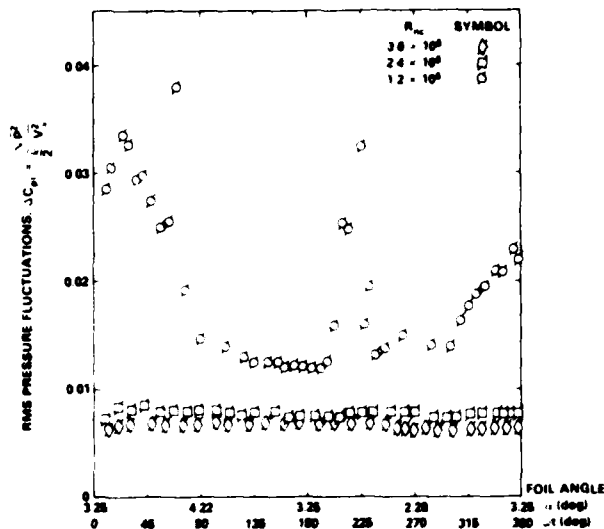


Figure 22 — Measured RMS Pressure Fluctuations at P_{25} with Three Reynolds Numbers and Oscillating Amplitude of 0.97 Degrees ($f = 10$ Hz)

5. INFLUENCE OF HYDROFOIL OSCILLATION ON CAVITATION INCEPTION

Let σ denote the vapor cavitation number:

$$\sigma = \frac{P_{\infty} - P_v}{\frac{1}{2} \rho V_{\infty}^2} \quad (10)$$

where P_v is the vapor pressure. If thermodynamic equilibrium prevails, then

$$\sigma = -C_{p_{min}} \quad (11)$$

at cavitation inception in pure fluids.² In practice significant deviation from this equation has been widely observed in the model cavitation tests. Arndt²⁶ stated that the so-called scale effects are due to deviations in two basic assumptions inherent in the cavitation scaling law; namely that the pressure scales with velocity squared and the critical pressure for inception is the vapor pressure. In practice, these two factors are interrelated, since the critical pressure is a function of the time scale of the pressure field. Consequently, depending on the cavitation resistance of the liquid, cavitation inception on the model may occur either (a) at the location of $C_{p_{min}}$, or (b) in the natural transition or laminar separation region of the model.¹²

5.1 Cavitation Inception at $C_{p_{min}}$

We will first consider the case when cavitation inception on the model occurs at the location of $C_{p_{min}}$. Since the magnitude of pressure fluctuations associated with a laminar flow is essentially zero, the present experiments show that

the flow at 3.3 percent chord length is laminar for all of the dynamic runs so that $\Delta C_{pt} = 0$. Theoretical computations $\alpha = 3.25^\circ$ show that $C_{p_{min}}$ occurs around $x/c = 0.018$; see Figure 3. Thus, Equation (9) reduces to:

$$\begin{aligned} C_p(t) &= C_{ps} + C_{pu}(t) \\ &= C_{ps} + |\Delta C_{pu}| \sin(\omega t + \phi) \end{aligned} \quad \text{for } 0 \leq x/c \leq 0.033 \quad (12)$$

where $|\Delta C_{pu}|$ and ϕ are the amplitude and phase angle.

An earlier series of experiments conducted by Shen and Peterson¹⁹ reported measured values of the dynamic pressure coefficient $C_p(t)$. Fully wetted, time dependent, experimental pressure distributions were compared with results from Giesing's method²⁷ for calculating unsteady potential flow. Good correlation between the predictions and the experimental measurements was obtained for both dynamic pressure amplitude and phase angle within the range of reduced frequencies investigated ($K = 0.23$ to 2.30)

Let σ_{is} and σ_{iu} denote the steady and unsteady inception angles, respectively. Let $\xi(K)$ be the ratio of dynamic angular pressure gradient $(dC_p/d\alpha)_u$ versus static angular pressure gradient $(dC_p/d\alpha)_s$ at a given location on the foil, namely:

$$\xi(K) = \frac{(dC_p/d\alpha)_u}{(dC_p/d\alpha)_s} \quad (13)$$

Based on Equation (12), Shen and Peterson showed that the unsteady inception angle σ_{iu} for a given reduced frequency K can be obtained from:

$$\begin{aligned} \sigma_{iu} &= \sigma_0 + (\sigma_{is} - \sigma_0) \frac{\cos \phi}{\xi} \\ &- \sigma_1 \sin \phi \sqrt{1 - \left(\frac{\sigma_{is} - \sigma_0}{\sigma_1 \xi} \right)^2} \quad (\sigma_1 \neq 0) \end{aligned} \quad (14)$$

The Shen and Peterson¹⁹ experimental results showed that cavitation inception always initiated around $x/c = 0.02$. This result is in good agreement with the assumption that cavitation inception occurs at the location of $C_{p_{min}}$. Due to a phase shift in the pressure distribution, a significant delay in inception of leading edge cavitation was observed with the foil in oscillation. It was concluded¹⁹ that the influence of hydrofoil oscillation on inception at $C_{p_{min}}$ of leading edge sheet cavitation can be reasonably predicted by Equation (14).

It is remarked that full-scale propellers are generally associated with high Reynolds numbers. The locations of boundary layer transition and $C_{p_{min}}$ may be coincided.¹² In this case, the pressure fluctuation term ΔC_{pt} must be added in Equation (12).

5.2 Cavitation Inception at Transition

We now consider the second case, when cavitation inception occurs in the transition region of the model. Aside from the pressure field, cavitation also requires a time scale in order for nuclei to grow. Experiments on axisymmetrical bodies by Arakeri and Acosta,⁹ and Huang⁴ showed that cavitation inception can occur in the boundary layer transition region when the value of $(-C_{ps} - \Delta C_{pt})$ is smaller than $-C_{p_{min}}$. Huang and Peterson¹² in dealing with steady cavitation assumed that:

$$\sigma_M = -C_{ptr} - \Delta C_{pt}$$

where α_M and \tilde{C}_{pt} are model cavitation inception numbers and potential flow pressure coefficients, respectively. On the other hand cavitation inception at full scale was assumed to occur when $\alpha_F = -C_{pmin}$. The difference in these two assumptions is due to time scale associated with bubble growth and flow regime associated with boundary layer pressure fluctuations.

Consider a previously discussed dynamic run with an oscillation amplitude of 1.57 deg, frequency of 5.5 Hz and free-stream speed of 9.75 m/s, corresponding to $R_{nc} = 2.4 \times 10^6$ and $k = 0.432$. This is a typical value of K for a surface ship propeller if the chord length at 0.7 radius is used as the characteristic length. The computed unsteady potential flow pressure coefficients $C_{ps} + C_{pd}(t)$ are shown in Figure 23 for several values of ωt ; see Table 2. The computations are based on Giesing's non-linear unsteady potential flow theory.²⁷ Recall that $\alpha = 3.25 + 1.57 \sin \omega t$. For purposes of comparison, the dynamic and static pressure distributions are shown in Figure 24. This figure gives $\alpha = 4.0$ degrees at $\omega t = 30$ degrees. At the same foil-geometric angle, due to the phase lag, the magnitude of the dynamic pressures is noticeably smaller than the static pressures near the leading edge. This result supports the experimental finding¹⁹ that leading edge sheet cavitation is delayed with the foil in oscillation; see Equation (14). The same trend has also been reported for aerodynamic stall.²⁸

Figure 5c suggests that the flow is in the final stage of transition at 10 percent chord, P_{10} for $R_{nc} = 2.4 \times 10^6$. Figure 15 shows that the pressure fluctuations due to advancing transition attain a maximum value at P_{10} around $\omega t = 30$ degrees. The measured rms pressure fluctuations give $\Delta C_{pt} = 0.0145$. Figure 7 shows that the measured frequently-occurring large negative pressure fluctuations are approximately 2.7 times larger than the rms value in the transition region. If cavitation occurs at the natural transition point of the model, we have $\alpha_M = 0.98 + 0.04 = 1.02$. A much higher value of $\Delta C_{pt} = 0.25$ may be used if transition is caused by laminar separation. This value of α_M is smaller than the value of $-C_{pmin}$. In the previous cavitation tests reported in Reference 19 with leading edge sheet cavitation, inception always occurred near the location of C_{pmin} . However, cavitation inception on axisymmetric bodies by Arakeri and Acosta, and Huang, did occur in the transition region where the quantity $(-C_{ptr} - \Delta C_{pt})$ is still smaller than $-C_{pmin}$.

Further studies required notably in three areas to determine: (1) why the magnitude of pressure fluctuation terms associated with natural transition and laminar separation are smaller in the present measurements than the values measured by Huang and Hannan¹⁰ with different instruments; (2) theoretically how the location of transition moves periodically with the foil in oscillation; and (3) the validity of the assumption used above that the location of transition measured at a steady mean foil angle is the critical location to trigger cavitation inception when the foil is in oscillation. This assumption requires further verification.

Two different types of cavitation inception phenomena have been considered in this study. One type is associated with cavitation inception at the location of C_{pmin} . The other type is associated with cavitation inception in the transition region. Headform experiments by Arakeri and Acosta,⁹ and Huang⁴ were correlated with the second type of cavitation inception. On the other hand, the leading-edge sheet cavitation on a hydrofoil observed by the present authors corresponds to the first type of inception. It is possible that a cambered hydrofoil with a smaller angle-of-attack, namely with a less severe suction pressure peak, could encounter cavitation inception at transition as observed by Kuiper²⁹ in his model propeller experiments.

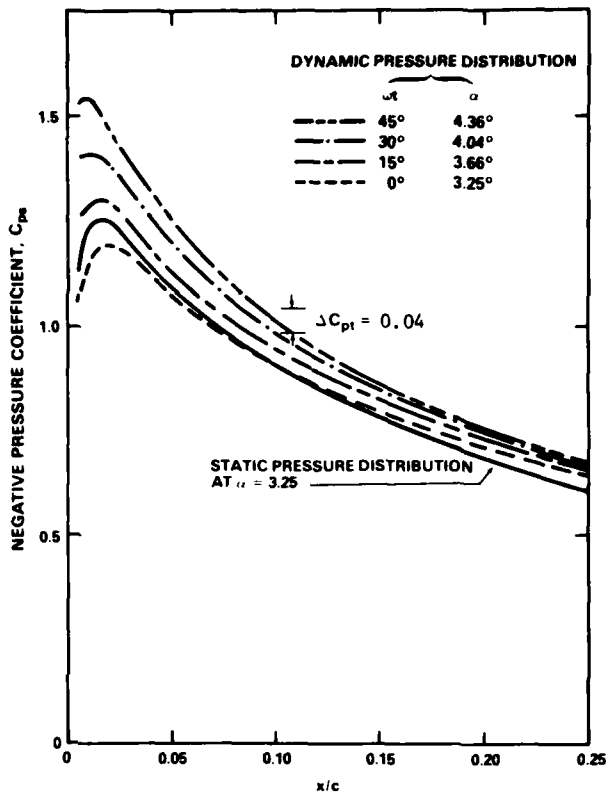


Figure 23 — Dynamic Pressure Distributions with $\alpha = 3.25 + 1.57 \sin \omega t$

x/c	° DEGREE	$(\frac{\partial C_p}{\partial x})_u$	$C_{pd}(t)$				
			-1	0	15	30	45
0.0073	10.0	21.0	0.100	0.050	0.197	0.330	0.441
0.0017	9.7	18.0	0.083	0.046	0.171	0.285	0.379
0.0118	9.1	15.3	0.068	0.044	0.150	0.246	0.325
0.026	8.3	13.0	0.051	0.043	0.132	0.213	0.280
0.035	7.5	11.3	0.040	0.040	0.118	0.188	0.246
0.056	5.2	8.5	0.021	0.040	0.099	0.149	0.190
0.100	2.6	5.2	0.006	0.031	0.066	0.096	0.120
0.250	20.7	2.7	0.026	0.043	0.057	0.067	0.073

$$K = 0.423, V_\infty = 9.75 \text{ m/s}, f = 5.5 \text{ Hz}, \alpha = 3.25 + 1.57 \sin \omega t$$

$$C_{pd}(t) = -\frac{\partial C_p}{\partial x} \sin \omega t + \alpha$$

TABLE 2 — DYNAMIC PRESSURE COEFFICIENT $C_{pd}(t)$

Due to the existence of these two different types of cavitation inception, Huang and Peterson¹² computed a significant scale effect. They provided a method for correcting model/full-scale propeller cavitation scaling in a steady flow. The present work is intended to provide needed information to compute cavitation scaling corrections in unsteady flow. It is shown that a diagram of mean pressure coefficient, C_{ps} and low frequency dynamic pressure coefficient, $C_{pd}(t)$

versus chordwise location must be constructed first. Secondly, the location of boundary layer transition with the foil in oscillation must be determined either theoretically or experimentally. Thirdly, the magnitude of boundary layer pressure fluctuations associated with frequently occurring negative pressure is determined. The selection of this magnitude depends on the Reynolds number and amplitude of oscillation angles as shown in Figures 8 to 24.

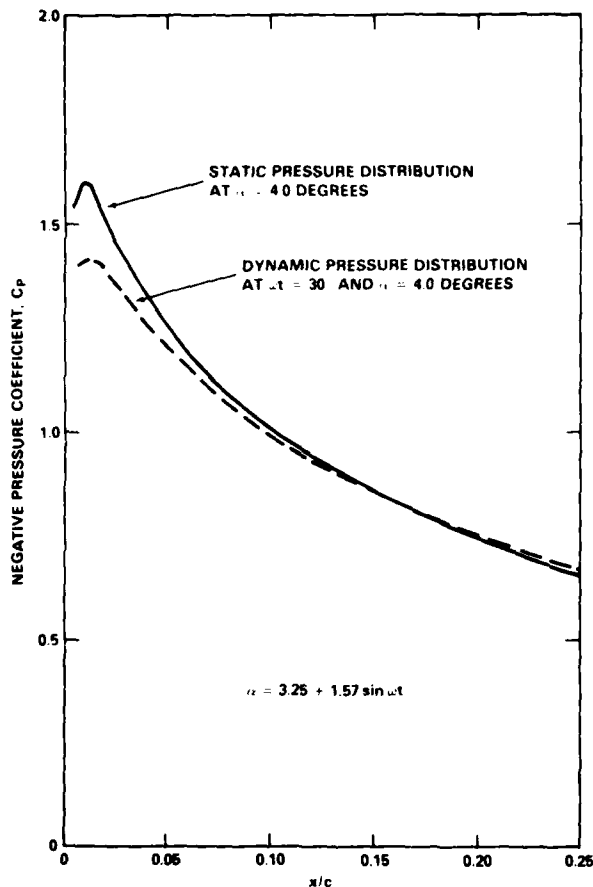


Figure 24 — Comparison of Dynamic and Static Pressure Distributions at $\alpha = 4.0$ Degrees

6. CAVITATION INSTABILITY AND NOISE

6.1 Foil Oscillation and Cloud Cavitation

Unsteady sheet cavitation has been recently reviewed by the 15th ITTC Cavitation Committee. The emphasis of this portion of the paper is on the salient features of sheet cavity instability. Tanibayashi³⁰ provided an insight into the subject

with his description of cavitation on a propeller in both uniform and nonuniform flow. He concluded that the presence of sheet and bubble cavitation in nonuniform flow can be predicted by quasi-steady methods, but that the collapse process cannot be predicted. Unfortunately, the details of the collapse process are the controlling factor in erosion, noise, and induced structural vibration. When the sheet cavity produces "cloud" cavitation, erosion, noise and vibration are observed to significantly increase in magnitude. For example, Chiba and Hoshimo³¹ found that the induced hull pressure had superimposed upon it pressure impulses produced by the cloud cavitation formed from the breakup of the propeller sheet cavity. A physical description of cloud cavitation and its formation has been given as follows:¹⁹

1. A large portion of the sheet cavity becomes highly distorted and undergoes a significant increase of overall cavity height in the distorted region.
2. Once this distorted region begins to separate from the main part of the sheet cavity, the upstream portion of the sheet cavity develops a smooth surface and reduced thickness.
3. The separated portion of the sheet develops the appearance of a cloud and moves downstream and expands away from the foil surface. The trailing edge of the smooth-surfaced region then moves downstream, becomes unstable at its trailing edge, and quickly develops the characteristic appearance of the leading edge sheet cavity elsewhere along the span. Alternately, the trailing edge of the smooth portion of the sheet cavity moves upstream to the foil leading edge as the cavity collapses and disappears. Photographs depicting this process can be found in reference 19.

Ito,³² reporting one of the first detailed experiments on the subject, compared unsteady cavitation on propellers in a wake field with pitching three dimensional hydrofoils. He concluded that the reduced frequency for the blade element of a propeller in a wake field has an important influence on the formation of cloud cavitation. The implication of Ito's work is that the wake field and the propeller should be considered together to minimize the adverse effects due to the formation of cloud cavitation.

Later work by Miyata, et al.¹⁶ with oscillating two-dimensional hydrofoils instrumented with surface mounted pressure gages showed that unsteady wing theory was useful in explaining the relationship between the time-dependent pressure distribution and cavitation. They concluded that the cavity collapse process is strongly influenced by the unsteadiness of the pressure field and the reduced frequency associated with foil oscillation.

The present authors¹⁹ provided further details on the instability of sheet cavitation and the formation of cloud cavitation. Their experiments were done with an oscillating two dimensional hydrofoil over a Reynolds number range from 1.2×10^6 to 3.6×10^6 and reduced frequencies up to 2.3. The results indicated that the principal controlling parameters were reduced frequency, K , cavitation number, σ , and foil oscillation amplitude, α_1 . The maximum cavity length, l_m/c , is a function of these three parameters and cannot be predicted on the basis of $K = 0$ conditions. The role of reduced frequency can be demonstrated in the following example.

For constant σ , it is possible to have marginal or no cloud cavitation at some finite K , even though it was present at the maximum unsteady angle when $K = 0$.

The importance of reduced frequency has also been shown by Matveyev and Gorshkoff.³³ They reported that for propellers in a uniform flow field, sheet cavitation was less noisy than bubble cavitation. However, when the propellers were in a nonuniform flow field, the sheet cavities become more unsteady and sheet cavitation then was noisier than bubble cavitation. As the work of Matveyev and Gorshkoff points out, it is of crucial importance that a similarity in cavitation time history exist between model and full scale. The noise scaling relations assume this similarity as a foundation and thus the importance of work such as reported by Bark and van Berlekom¹⁸ is reinforced.

Bark and van Berlekom tried to assess the cavitation noise produced by a propeller in nonuniform flow by studying the cavitation noise generated by a pitching hydrofoil. Based on a correlation of photos of cavity life cycles and their associated radiated noise, they concluded that good simulation of specific events is important and that these important events are not generally described by simple parameters (e.g. collapse time, T_c ; variation of cavity area with time, $A(t)$; and maximum cavity volume, V_{max}). One of the most important aspects of the process is the separation of the cavity (i.e. cloud cavitation formation) which must be correctly scaled. They found that cloud cavitation formation can occur at an early stage of the sheet cavity collapse. Furthermore, in agreement with the results of the present authors¹⁹ a combination of long (chordwise) cavity length and high reduced frequency causes extensive cloud cavitation. As can be concluded from the data presented in their paper, large noise transients were associated with the cloud cavitation.

6.2 Cloud Cavitation and Noise

The observed phenomena to be discussed in this paper can best be described by reference to examples shown in Figure 25. Table 3 summarizes all of the parameters associated with the tests reported here. To limit the scope of the test program, air content of the water was not varied. The air content was measured with 70 percent saturation in reference to atmospheric pressure at a water temperature of 22.2°C and tunnel pressure of 103.6 KPa. For a velocity of 16.4 m/s, $\alpha = 3.25 + 0.95 \sin \omega t$, $\sigma = 1.21$, a plot of relative sound power \bar{P}^2 versus K shows the existence of a "noise bucket." When $\alpha = 4.3^\circ$ and $K = 0$, extensive cloud cavitation is developing from the sheet cavity and the noise level is high. As the foil is oscillated, a leading edge sheet cavity experiences an inception, growth, and collapse cycle related to the impressed pressure distribution of the foil. At low reduced frequencies no cloud cavitation is produced, the sheet cavity collapses toward the foil leading edge, and there is a significant reduction in the noise relative to the condition of $\alpha = 4.3^\circ$ and $K = 0$. As the reduced frequency is increased further, a cloud cavity is produced during the collapse of the sheet cavity and the noise level again increases due to cloud cavitation collapses. This variation in \bar{P}^2 as a function of foil angle is shown in oscillograph records, Figure 26, for 2 foil oscillation periods and in Figure 27 as a mean noise variation based on the average of the cycles occurring in a 40 second period.

Figure 25 also presents data that demonstrate the strong dependence of \bar{P}^2 on the water velocity. For $\alpha = 4.3^\circ$, $K = 0$, and $\sigma = 1.13$, heavy cloud cavitation is present and

the noise level increases by a nominal factor of 30 when the velocity is increased from 11.5 m/s to 16.4 m/s. Once foil oscillation starts the amount of cloud cavitation is significantly reduced and the velocity difference appears to have far less impact on the radiated noise. At large K when the cloud cavitation is produced upon sheet cavity dependence, the

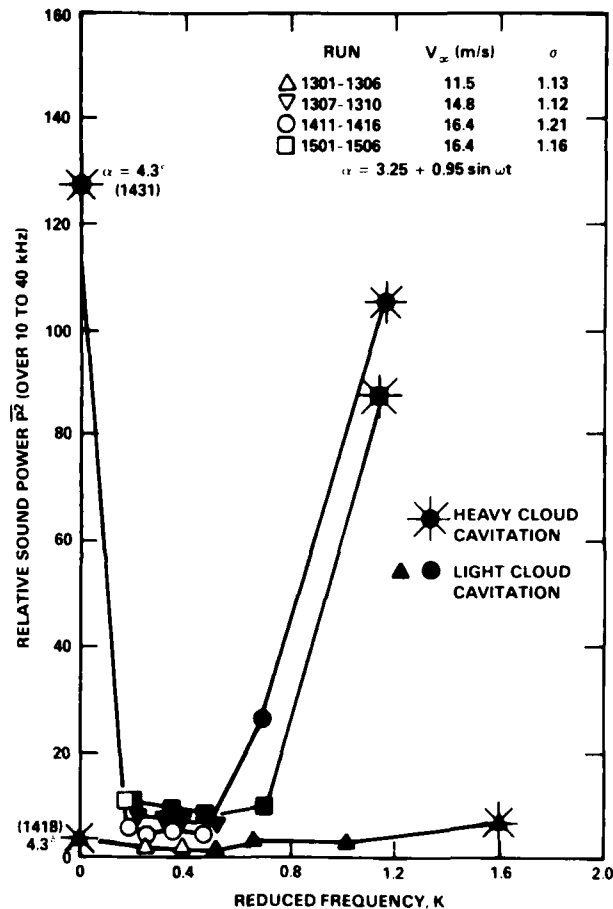


Figure 25 — Influence of V_∞ and Reduced Frequency on Relative Sound Power for $\alpha = 3.25 + 0.95 \sin \omega t$

strong influence of velocity is again apparent.

The influence of velocity on the radiated sound power is just as dramatic when the amplitude of oscillation is increased from 0.95 to 1.55 degrees, keeping σ constant, as shown in Figure 28. There it is seen that with the larger amplitude of oscillation cloud cavitation is present over the full range of reduced frequencies. Although the violence associated with the cloud cavitation at large reduced frequencies limited the ability to collect data, it is apparent that \bar{P}^2 has a strong dependence on K when the cloud cavitation is present. Reference to Figure 25 shows that this latter effect is not present when little or no cloud cavitation is present.

RUN NO.	V, m/s	$R_{\infty} \cdot 10^4$	f Hz	K		DEGREE
1301	11.49	2.8	4	0.264	1.13	0.95
1302	11.49	2.8	5.5	0.362	1.13	0.95
1303	11.49	2.8	7.5	0.494	1.13	0.95
1304	11.49	2.8	10	0.659	1.13	0.95
1306	11.49	2.8	15	0.988	1.13	0.95
1306	11.49	2.8	25	1.646	1.13	0.95
1307	14.78	3.6	4	0.205	1.12	1.00
1308	14.78	3.6	5.5	0.282	1.12	1.00
1309	14.78	3.6	7.5	0.384	1.12	1.00
1310	14.78	3.6	10	0.513	1.12	1.00
1401	11.49	2.8	4	0.264	1.13	1.55
1402	11.49	2.8	5.5	0.362	1.13	1.55
1403	11.49	2.8	7.5	0.494	1.13	1.55
1404	11.49	2.8	10	0.659	1.13	1.55
1406	11.49	2.8	15	0.988	1.13	1.55
1406	11.49	2.8	25	1.646	1.13	1.55
1407	14.78	3.6	4	0.205	1.14	1.55
1408	14.78	3.6	5.5	0.282	1.14	1.55
1409	14.78	3.6	7.5	0.384	1.14	1.55
1410	14.78	3.6	10	0.513	1.14	1.55
1411	16.42	4.0	4	0.185	1.21	0.95
1412	16.42	4.0	5.5	0.254	1.21	0.95
1413	16.42	4.0	7.5	0.346	1.21	0.95
1414	16.42	4.0	10	0.461	1.21	0.95
1415	16.42	4.0	15	0.691	1.21	0.95
1416	16.42	4.0	25	1.153	1.21	0.95
1418	11.49	2.8	0	0	1.12	4.25°
1431	16.42	4.0	0	0	1.21	4.30°
1501	16.42	4.0	4	0.185	1.15	0.95
1502	16.42	4.0	5.5	0.255	1.15	0.95
1503	16.42	4.0	7.5	0.347	1.15	0.95
1504	16.42	4.0	10	0.462	1.15	0.95
1506	16.42	4.0	15	0.694	1.15	0.95
1506	16.42	4.0	25	1.153	1.15	0.95
1508	16.42	4.0	0	0	0.93	3.25°
1509	16.42	4.0	0	0	0.93	3.45°
1510	16.42	4.0	4	0.185	0.93	0.32
1511	16.42	4.0	5.5	0.254	0.93	0.32
1512	16.42	4.0	7.5	0.346	0.93	0.32
1513	16.42	4.0	10	0.462	0.93	0.32
1514	16.42	4.0	15	0.694	0.93	0.32
1515	16.42	4.0	25	1.153	0.93	0.32

TABLE 3 - TEST RUN NUMBERS AND ASSOCIATED PARAMETERS

The variation in \bar{P}^2 during the foil oscillation period is shown by oscillograph records in Figure 29 and as a mean variation based on the average of the cycles occurring in a 40 second period in Figure 30. Based on the limited data presented in Figures 25 to 30, it appears that for cloud cavitation originating from an unstable leading-edge sheet cavity $\bar{P}^2 \sim V_{\infty}^4$ when α , K, σ_0 , σ_1 are constant.

The maximum cavity volume, area coverage, etc., of a leading edge sheet cavity have in the past been used as parameters associated with the magnitudes of the cavitation noise. Figure 31 presents the maximum length achieved by the leading edge sheet cavity as a function of the reduced frequency. From these data and the noise data of Figure 25, it is clear that the maximum cavity length has essentially no cor-

relation with \bar{P}^2 . This basic conclusion was also deduced by Bark and Berlekom.¹⁸ As has already been shown, the principal source of noise is the collapse of the cloud cavitation generated by the sheet cavity. As shown in Figure 32, for small reduced frequencies, the sheet cavity disappears after the radiated noise level has peaked. However, as the reduced frequency is increased and the formation of cloud cavitation is progressively delayed until it occurs at the sheet cavity desinent condition, the peak amplitude of the noise occurs after the sheet cavity has disappeared. In fact, for the reduced frequency of 1.65, maximum radiated noise does not occur until the foil reaches its minimum angle of attack. Before the cloud cavitation completely disappears, the inception of a new leading edge sheet cavity has occurred.

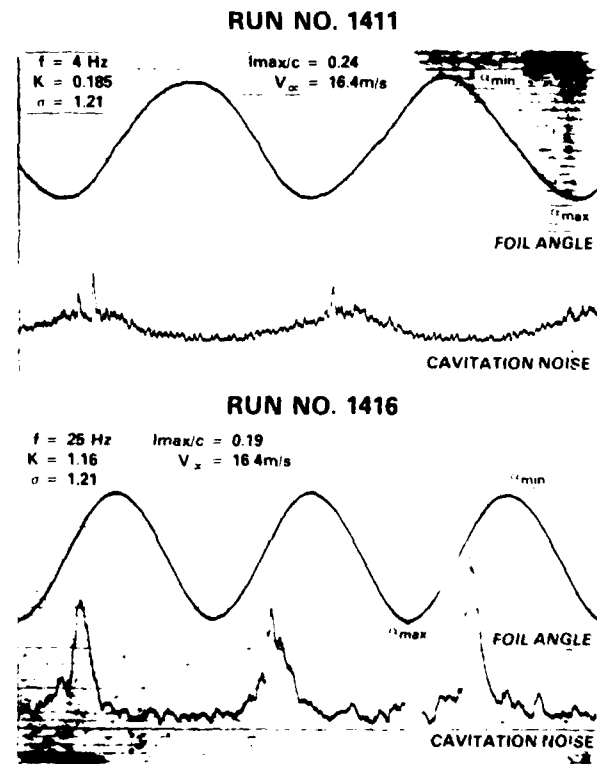


Figure 26 - Cavitation Noise Signals $\sqrt{P^2}$ and Foil Angles for Runs 1411 and 1416, $\alpha = 3.25 + 0.95 \sin \omega t$

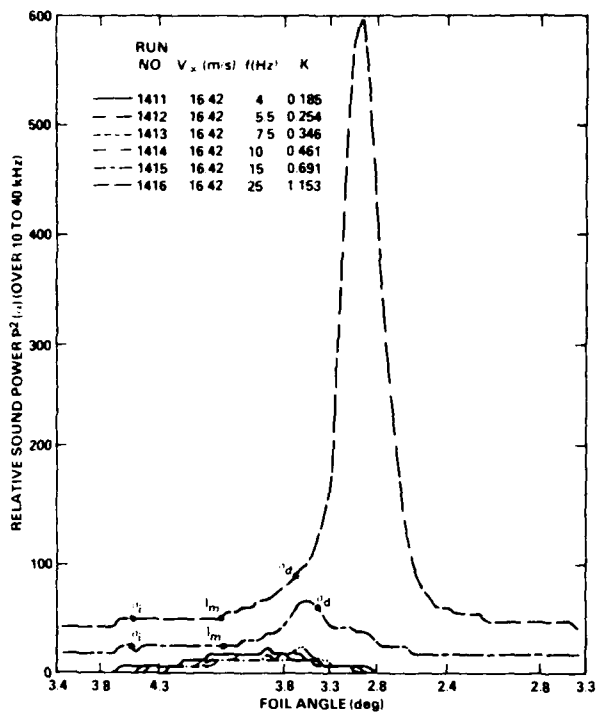


Figure 27 - Relative Sound Power $\bar{P}^2(\alpha)$ as a Function of Foil Angle for Runs 1411 to 1416 with σ_1 , I_m & α_d for Sheet Cavitation

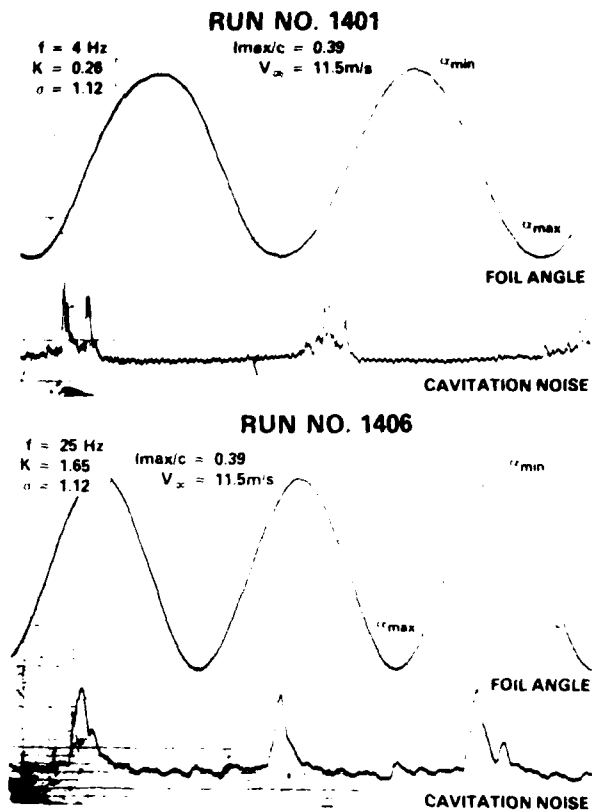


Figure 29 - Cavitation Noise Signals $\sqrt{P^2}$ and Foil Angles for Runs 1401 and 1406, $\alpha = 3.25 + 1.55 \sin \omega t$

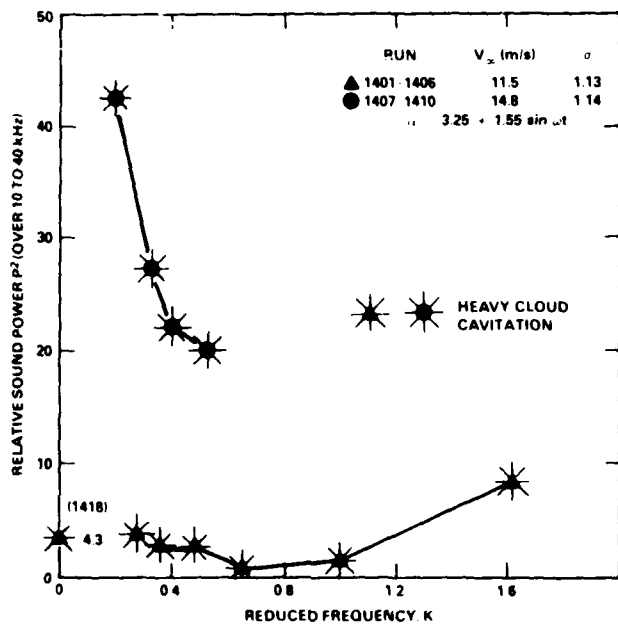


Figure 28 - Influence of V_∞ and Reduced Frequency on Relative Sound Power for $\alpha = 3.25 + 1.55 \sin \omega t$

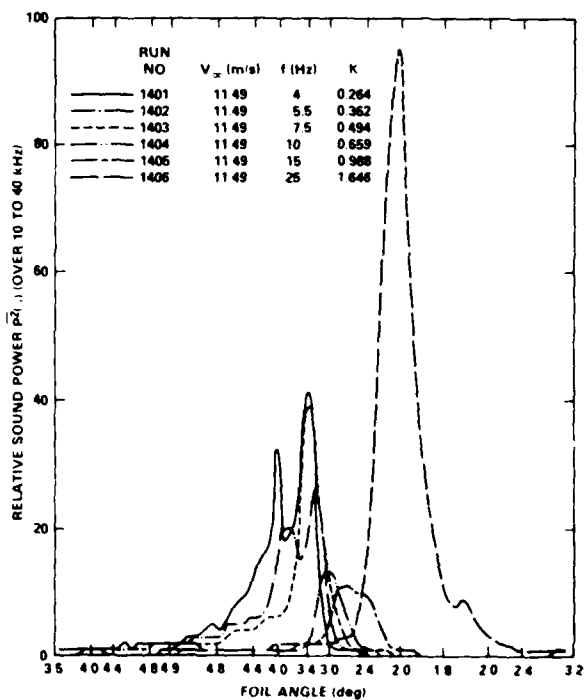


Figure 30 - Relative Sound Power $\bar{P}^2(\alpha)$ as a Function of Foil Angle for Runs 1401 to 1406

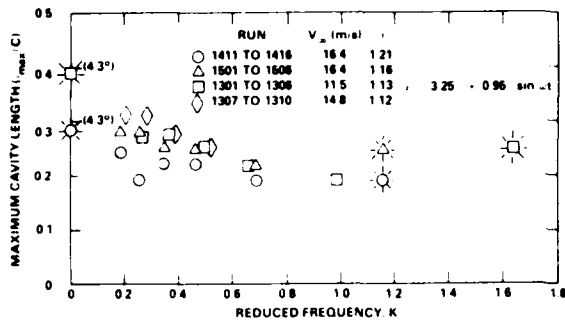


Figure 31 — Measured Maximum Cavity Length vs. Reduced Frequency

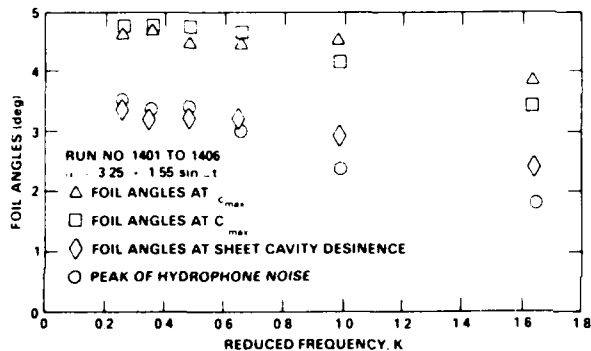


Figure 32 — Measured Foil Angles at Maximum Lift, Maximum Cavity Length, Noise Peak and Leading Edge Sheet Cavity Desinence for Runs 1401 to 1406

In many instances, partially cavitating hydrofoils are subjected to conditions that can be effectively simulated by small amplitude oscillation during which the leading edge sheet cavitation is continuously present. Based on results for the intermittent sheet cavity, it is known that sheet cavity stability, and hence propensity to produce cloud cavitation, is dependent on the reduced frequency. The noise level variation associated with this type of cavitation is found in Figure 33. As with intermittent sheet cavitation, the noise level is low when cloud cavitation is not present. Once cloud cavitation forms, then there is a dramatic increase in the mean sound power level and in the time variation of sound power level, as shown in Figures 33 and 34 respectively. It is apparent from these results that the desinent condition for the sheet cavity is not required for high radiated noise levels, but rather the existence of conditions that promote the formation of cloud cavitation.

If a leading edge sheet cavity is considered as similar to separated flow at a foil's leading edge, then some parallels can be drawn with the vast body of recently published data on dynamic stall. For example, the following conclusion from McAlister and Carr³⁴ closely parallels the description of cavity stability given by Shen and Peterson.¹⁹

"The free-shear layer that was created between the region of reversed flow and the inviscid stream was not stable. This instability resulted in a transformation of the free-shear layer into a multitude of discrete clockwise vortices, 'out of which emerged a dominant 'shear-layer vortex'." McAlister and Carr go on to further describe the

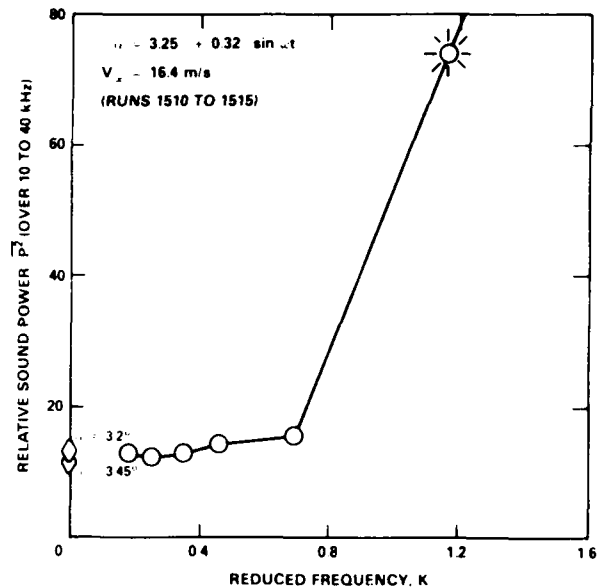
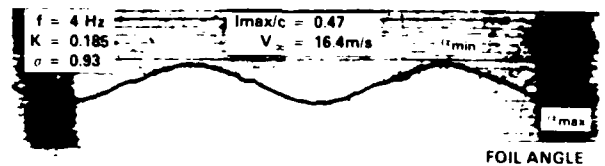


Figure 33 — Relative Sound Pressure \bar{P}^2 Over One Cycle for a Continuously Cavitating Hydrofoil

RUN NO. 1510



RUN NO. 1515

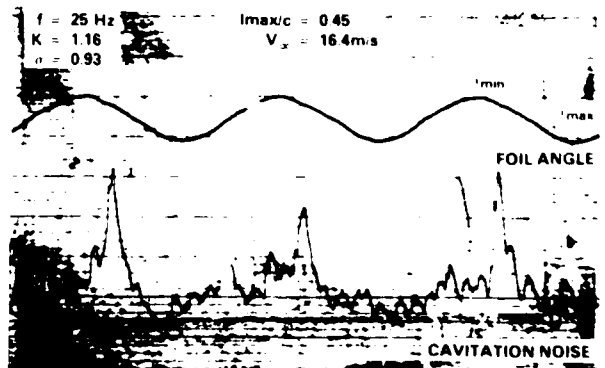


Figure 34 — Cavitation Noise Signals $\sqrt{P^2}$ and Foil Angles for Runs 1510 and 1515, $\alpha = 3.25 + 0.32 \sin \omega t$

upstream movement of a thin layer of reversed flow along the foil surface. When this reversed flow reached the leading edge, "... a protuberance appeared over the first 6 percent of the surface in response to the sudden influx of fluid. This protuberance grew and eventually developed into the 'dynamic-stall vortex' that has been observed in high Reynolds number experiments." This dynamic stall vortex moves downstream and away from the airfoil surface just as cloud cavitation does on a cavitating hydrofoil. Furthermore, if the location of flow reversal is plotted against airfoil angle,³⁴ it is seen that foil oscillation (i.e. $K = 0.25$) will suppress the forward movement of the reversed flow region. This is again similar to the cavity stabilization at low reduced frequencies relative to the stationary hydrofoil.

These types of analogies must be used with great care. For example, one of the conclusions of Telionis and Koromilas³⁵ from their study of unsteady laminar separation is that separation is not affected by the amplitude of oscillation. The parallel with cavitating flows may break down here due to, among other reasons, the inertial considerations of growing cavities. Telionis and Koromilas also have concluded that for finite oscillation frequencies, the point of reverse flow is shifted downstream from the quasi-steady location.

7. CONCLUDING REMARKS

Depending on the cavitation resistance of the liquid, cavitation inception on a model may occur either (1) at the location of C_{pmin} , or (2) in the transition region of the model. In the present experiments for a hydrofoil with a large suction peak, leading edge sheet cavitation was observed to take place at C_{pmin} . In this case, the boundary layer was laminar at the location of C_{pmin} and an unsteady potential flow theory was shown to provide a good correlation between prediction and experimental measurements of cavitation inception.

For the case of cavitation occurring in a transition region, it is shown that a diagram of mean pressure coefficient and low frequency dynamic pressure coefficient versus chordwise location must be constructed first. Secondly, the location of boundary layer transition with the foil in oscillation must be determined either theoretically or experimentally. Thirdly, the magnitude of boundary layer pressure fluctuations associated with frequently occurring negative pressure is determined. A general theory on boundary layer properties with a hydrofoil in oscillation is not yet available. The present work is intended to provide some needed information on this subject: the location of transition and the magnitudes of boundary layer pressure fluctuations. Experimental results show:

1. The movement of boundary layer transition can be detected by the measurement of pressure fluctuations on the foil surface.
2. The development of the foil's boundary layer is delayed with an increase in oscillation frequency.
3. The pressure peaks associated with advancing transition are independent of oscillation amplitude and frequency and are identical with the values measured in the transition regions on a stationary foil.
4. In a fully established turbulent region, the magnitudes of pressure fluctuations are independent of oscillation amplitude and frequency and identical with the values measured in the turbulent region on stationary foil.
5. The magnitude of pressure fluctuations measured on the present foil gives higher intensity in a

natural transition region than in a fully established turbulent region.

With respect to cavitation noise the following conclusions were derived from water tunnel hydrophone measurements:

1. The stability of a leading edge sheet cavity determines the extent to which cloud cavitation is produced.
2. The formation of cloud cavitation during the life of a sheet cavity is suppressed at small reduced frequencies and correspondingly the noise level is low.
3. At high reduced frequencies, extensive cloud cavitation is formed during the final phase of sheet cavity collapse and the noise level is significantly increased. Thus P^2 plotted against K shows a "noise bucket." When the sheet cavity is continuous with time, a similar noise bucket is apparent.
4. When σ , K , α_0 , and α_1 are kept constant, the influence of velocity on P^2 is found to be very large if cloud cavitation is present. From the limited data obtained from these experiments, the sound power associated with cloud cavitation appears to vary as:

$$P^2 \sim V_0^8$$

5. The amplitude of oscillation, α_1 , has an influence on the noise in that larger amplitudes promote cloud cavitation formation. However, the limited data available do not permit more detailed discussion of this point.
6. The cavitation noise generated by a stationary foil is not indicative of the noise produced when the foil is oscillated.
7. The reduced frequency parameter, K , does not include consideration of gross cavity dynamics. Thus it is not sufficient to predict the influence of free-stream velocity on the gross stability of the leading edge sheet cavity. This influence of velocity should be investigated further in order to establish the critical K at which the radiated noise increases at full scale speeds.

The subject of unsteady cavitation is a topic just in its embryonic state of understanding. Recent research confirms what has been empirically observed for many years, that is, reasonable simulation of erosion, noise and induced hull vibration requires a simulation of the flow field in which the hydrofoil or propeller operates. A propeller operated in uniform flow cannot simulate some of the critical details of the inception, growth and collapse process of leading edge sheet cavities.

ACKNOWLEDGMENTS

The authors would like to thank Mr. Robert Pierce for his assistance in the data processing. His development of new techniques allowed a much more quantitative evaluation than would otherwise have been possible. The assistance given by Mrs. Nancy Groves in linear stability calculations of laminar boundary layer is greatly appreciated.

The work reported herein was funded by the Naval Sea Systems Command, Code 035, under the General Hydrodynamic Research Program, Element 61153N, Task Area SR 0230101.

REFERENCES

1. Peterson, F.B. and R.E. Arndt, "Unsteady Cavitation," 19th American Towing Tank Conference, University of Michigan, Ann Arbor, July 1980
2. Acosta, A.J. and B.R. Parkin, "Report of the ATTC Cavitation Inception Committee," 19th American Towing Tank Conference, University of Michigan, Ann Arbor, July 1980
3. Acosta, A.J. and B.R. Parkin, "Cavitation Inception - A Selective Review," *Journal of Ship Research*, Vol. 19, No. 4, Dec. 1975, pp. 193-205
4. Huang, T.T., "Cavitation Inception Observations on Six Axisymmetric Headforms," paper presented at the ASME International Symposium on Cavitation Inception, New York, Dec. 2-7, 1979
5. Rouse, H., "Cavitation in the Mixing Zone of a Submerged Jet," *La Houille Blanche*, Jan.-Feb. 1973, pp. 9-19
6. Daily, J.W. and V.E. Johnson, "Turbulence and Boundary Layer Effects on Cavitation Inception from Gas Nuclei," *Trans. ASME*, Vol. 78, 1956, pp. 1695-1706
7. Levkovskii, Y.L. and A.V. Chalov, "Influence of Flow Turbulence on the Inception and Growth of Cavitation," *Sov. Phys. Acoust.* 24(2), March-April 1978 (English Translation)
8. Arakeri, V.H. and A.J. Acosta, "Viscous Effects in the Inception of Cavitation on Axisymmetric Bodies," *Trans. ASME, Journal of Fluids Engineering*, Vol. 95, Series 1, No. 4, Dec. 1973, pp. 519-527
9. Arakeri, V.H. and A.J. Acosta, "Cavitation Inception Observations on Axisymmetric Bodies at Supercritical Reynolds Numbers," *Trans. ASME, Journal of Fluid Engineering*, Vol. 97, Series 1, 1975, pp. 82-87
10. Huang, T.T. and D.E. Hannan, "Pressure Fluctuation in the Regions of Flow Transition," David W. Taylor Naval Ship Research and Development Center Report 4723, 1976
11. Arakeri, V.H., "A Note on the Transition Observations on an Axisymmetric Body and Some Related Fluctuating Wall Pressure Measurements," *Journal of Fluids Engineering*, *Trans. ASME*, Vol. 97, Series 1, No. 1, March 1975, pp. 82-86
12. Huang, T.T. and F.B. Peterson, "Influence of Viscous Effects on Model/Full Scale Cavitation Scaling," *Journal of Ship Research*, Vol. 20, Dec. 1976, pp. 215-223
13. DeMetz, F.C., Farabee, T.M. and M.J. Casarella, "Statistical Features of the Intermittent Surface Pressure Field in a Transition Boundary Layer," *Trans. ASME, Non-steady Fluid Dynamics*, Edited by D.E. Crow and J.A. Miller, 1978, pp. 33-39
14. DeMetz, F.C. and M.J. Casarella, "An Experimental Study of the Intermittent Properties of the Boundary Layer Pressure Field During Transition on a Flat Plate," NSRDC, Report No. 4140, Nov. 1973
15. Gedney, C.J., "Wall Pressure Fluctuations During Transition on a Flat Plate," M.I.T., Acoustic and Vibration Laboratory Report No. 84618-1, April 1979
16. Miyata, H. et al., "Pressure Characteristics and Cavitation on an Oscillating Hydrofoil," *Journal of the Society of Naval Architects of Japan*, Vol. 132, No. 10, 1972, pp. 107-115
17. Radhi, M.H., "Theoretische und Experimentelle Untersuchung über den Kavitationseinsatz an Schwingenden Tragflügelprofilen," PhD Thesis, Technischen Universität Berlin, D83, 1975
18. Bark, G. and W. van Berlekom, "Experimental Investigations of Cavitation Noise," 12th Symposium on Naval Hydrodynamics, Washington, D.C., June 1978, pp. 470-493
19. Shen, Y.T. and F.B. Peterson, "Unsteady Cavitation on an Oscillating Hydrofoil," 12th Symposium on Naval Hydrodynamics, Washington, D.C., June 1978, pp. 362-384
20. Van Houten, R.J., "The Transient Cavitation on a Two-Dimensional Hydrofoil - Comparison of Theory and Experiment," M.I.T. Department of Ocean Engineering, OSP 87268, Aug. 1979
21. Hilten, J.S., et al., "A Simple Sinusoidal Hydraulic Pressure Calibration," National Bureau of Standards, Technical Note 720, 1972
22. Smith, A.M.O., "Transition, Pressure Gradient, and Stability Theory," *Proceeding of the Ninth International Congress of Applied Mechanics*, Brussels, Belgium, Vol. 4, 1957, pp. 234-243
23. Burton, T.E., "Wall Pressure Fluctuations at Smooth and Rough Surfaces Under Turbulent Boundary Layers With Favorable and Adverse Pressure Gradients," M.I.T. Acoustic and Vibration Laboratory, Report No. 70208-9
24. Ludwig, H. and W. Tillman, "Untersuchungen über die Wandschubspannung in Turbulenten Reibungsschichten," *Ing.-Arch* 17, 1949, pp. 288-299, (English translation) in NACA TM 1285, 1950
25. Blake, W.K., "Turbulent Boundary-Layer Wall Pressure Fluctuations on Smooth and Rough Walls," *Journal of Fluid Mechanics*, Vol. 44, 1970, pp. 637-660
26. Arndt, R.E. and W.K. George, "Pressure Fields and Cavitation in Turbulent Shear Flows," 12th Symposium on Naval Hydrodynamics, Washington, D.C., June 1978, pp. 327-339
27. Giesing, J.P., "Two-Dimensional Potential Flow Theory for Multiple Bodies in Small-Amplitude Motion," Douglas Aircraft Company, Report No. DAC-67028, April 1968
28. McCroskey, W.J., "Some Current Research in Unsteady Fluid Dynamics - the 1976 Freeman Scholar Lecture," *Trans. ASME, Journal of Fluid Engineers*, Vol. 99, Series 1, March 1977, pp. 8-38

29. Kuiper, G., "Scale Effects on Propeller Cavitation Inception," 12th Symposium on Naval Hydrodynamics, Washington, D.C., June 1978

30. Tanibayashi, H., "Practical Approach to Unsteady Problems of Propellers," Pro. Second Lips Propeller Symposium, May 10-11, 1973, pp. 65-78

31. Chiba, N. and T. Hoshino, "Effect of Unsteady Cavity on Propeller Induced Hydrodynamic Pressure," Journal of the Society of Naval Architects of Japan, 139, 1976

32. Ito, T., "An Experimental Investigation into the Unsteady Cavitation of Marine Propellers," Proceedings of IAHR - Symposium on Cavitation and Hydraulic Machinery, Sendai, Japan, 1962

33. Matveyev, G.A. and A.S. Gorshkoff, "Cavitation Noise Modelling at Ship Hydrodynamic Laboratories," 12th Symposium on Naval Hydrodynamics, Washington, D.C., June 1978

34. McAlister, K.W. and L.W. Carr, "Water Tunnel Visualization of Dynamic Stall," Trans. ASME, Journal of Fluids Engineering, 101, September 1979, pp. 276-380

35. Telonis and Koromilas, "Flow Visualization of Transient and Oscillatory Separating Laminar-Flow," Trans. ASME, Nonsteady Fluid Dynamics, Edited by D.E. Crow and J.A. Miller, 1978, pp. 21-32

INITIAL DISTRIBUTION

Copies		Copies	
1	WES		NAVSEA (Continued)
1	U.S. ARMY TRAS R&D Marine Trans Div		1 SEA 05T
1	CHONR/438 Cooper		1 SEA 05H
2	NRL		1 SEA 312
	1 Code 2027		1 SEA 32
	1 Code 2629		1 SEA 321
1	ONR/Boston		1 SEA 32R
1	ONR/Chicago	12	1 SEA 521
1	ONR/New York	1	1 SEA 524
1	ONR/Pasadena	1	1 SEA 62P
1	ONR/San Francisco	2	1 SEA 6661, Blount
1	NORDA		3 SEA 996
3	USNA		DTIC
	1 Tech Lib		1 AFOSR/NAM
	1 Nav Sys Eng Dept		1 AFFOL/FYS, J. Olsen
	1 B. Johnson		2 MARAD
3	NAVPGSCOL		1 Div of Ship R&D
	1 Lib		1 Lib
	1 T. Sarpkaya		1 NASA/HQ/Lib
	1 J. Miller		1 NASA/Ames Res Ctr, Lib
1	NADC		1 NSF/Eng Lib
1	NOSC/Lib	2	MMA
1	NSWC, White Oak/Lib		1 National Maritime Research Center
1	NSWC, Dahlgren/Lib		1 Lib
1	NUSC/Lib	1	U. of Cal/Dept Naval Arch, Berkeley
15	NAVSEA		1 Lib
	1 SEA 033	1	CIT
	1 SEA 03D		1 Aero Lib
		1	Colorado State U./Eng Res Cen
		1	Cornell U./Shen, S.F.

Copies

1 Harvard U.
1 Gordon McKay Lib

1 U. of Iowa
1 Lib

1 MIT
1 Lib

1 U. of Minn/St. Anthony Falls

1 U. of Mich/NAME
1 Lib

1 Penn State ARL Lib

1 Science Application, Inc.
Annapolis, MD
C. Von Kerczek

1 SIT
1 Lib

1 Stanford U.
1 Eng Lib

1 U. of Virginia/Aero Eng Dept

1 VPI
1 J. Schetz, Dept Aero &
Ocean Eng

1 Webb Inst
1 Lib

1 SNAME/Tech Lib

1 Boeing Company/Seattle
1 Marine System

1 Exxon, NY/Design Div
Tank Dept

1 General Dynamics, EB/
Boatwright

1 Flow Research

1 Gibbs & Cox/Tech Info

Copies

1 Grumman Aerospace Corp/Lib

1 Hydronautics
1 Lib

1 Lockheed, Sunnyvale/Waid

1 Sun Shipbuilding/Chief
Naval Arch

1 Westinghouse Electric
1 M.S. Macovsky

CENTER DISTRIBUTION

Copies	Code	Name
1	1500	W.B. Morgan
1	1502	V.J. Monacella
1	1520	W.C. Lin
1	1524	W. Day
1	1532	M. Wilson
1	154	J. McCarthy
1	1542	B. Yim
1	1543	R. Cumming
1	1544	T. Brockett
1	1544	R. Boswell
1	1544	K.F. Lin
1	1552	T.T. Huang
20	1552	Y.T. Shen
1	1552	N.C. Groves
1	1552	H.T. Wang
1	1552	M.S. Chang
1	1561	C.M. Lee
1	1564	J. Feldman
1	1568	G. Cox
1	1606	T.C. Tai
1	1840	J. Schot
1	1843	H. Hausling

Copies	Code	Name
1	19	M.M. Sevik
1	1940	J.T. Shen
1	1942	F. Archibald
1	1942	B.E. Bowers
1	1946	J.A. Padgett
10	5211.1	Reports Distribution
1	522.1	Unclassified Lib (C)
1	522.2	Unclassified Lib (A)



**LATE
LME**